

Can AI be enabled to dynamical downscaling? A Latent Diffusion Model to mimic km-scale COSMO5.0_CLM9 simulations

Elena Tomasi¹, Gabriele Franch¹, and Marco Cristoforetti¹

¹Data Science for Industry and Physics, Fondazione Bruno Kessler, via Sommarive 18, 38123, Trento (TN), Italy

Correspondence: Elena Tomasi (eltomasi@fbk.eu)

Abstract. Downscaling techniques are one of the most prominent applications of Deep Learning (DL) in Earth System Modeling. A robust DL downscaling model can generate high-resolution fields from coarse-scale numerical model simulations, saving the timely and resourceful applications of regional/local models. Additionally, generative DL models have the potential to provide uncertainty information, by generating ensemble-like scenario pools, a task that is computationally prohibitive for traditional numerical simulations. In this study, we apply a Latent Diffusion Model (LDM) to downscale ERA5 data over Italy up to a resolution of 2 km. The high-resolution target data consists of 2-m temperature and 10-m horizontal wind components from a dynamical downscaling performed with COSMO_CLM. Our goal is to demonstrate that recent advancements in generative modeling enable DL to deliver results comparable to those of numerical dynamical models, given the same input data, preserving the realism of fine-scale features and flow characteristics. A selection of predictors from ERA5 is used as input to the LDM, and a residual approach against a reference UNET is leveraged in applying the LDM. The performance of the generative LDM is compared with reference baselines of increasing complexity: quadratic interpolation of ERA5, a UNET, and a Generative Adversarial Network (GAN) built on the same reference UNET. Results highlight the improvements introduced by the LDM architecture and the residual approach over these baselines. The models are evaluated on a yearly test dataset, assessing the models' performance through deterministic metrics, spatial distribution of errors, and reconstruction of frequency and power spectra distributions.

1 Introduction

High-resolution near-surface meteorological fields such as 2-m temperature and 10-m wind speed are key targets for the weather and climate scientific and operational communities. Such high-resolution information is of essential importance for a wide variety of applications (e.g. available wind potential, predicted energy consumption, etc.), across diverse timescales, from weather forecasting (nowcasting, medium-range forecasting, and seasonal predictions) to climate projections. The hunger for high-resolution data is directly linked to and justified by the information that such data hold: extreme weather events and localized phenomena can typically be described by highly resolved fields only.

Downscaling is a well-known approach that allows obtaining local high-resolution data (predictands) starting from low-resolution information (predictors) by applying suitable refinement techniques. The two most traditional approaches are dy-

namical downscaling and statistical downscaling (Hewitson and Crane, 1996; Wilby and Wigley, 1997; Maraun and Widmann, 2018), applied alternatively depending on the final goal of each specific application.

Traditionally, high-resolution fields are achieved in operational weather forecasting by performing dynamical downscaling of lower-resolution simulations. Examples of this approach are all the Local Area Models (LAMs) run in every operational center worldwide, fed with global circulation models at a low resolution, and producing high-resolution fields for a localized area, typically nationwide (e.g., Baldauf et al., 2011; Seity et al., 2011; ARPAE-SIMC). As for the climate community, this approach materializes, for example, in applications run within the WCRP Coordinated Regional Downscaling Experiment (CORDEX, Giorgi et al. (2009)), performing dynamical downscaling of climate projections with Regional Climate Models (RCM) going from the ~ 100 -km resolution of Global Climate Models (GCM) down to a ~ 16 -km resolution (e.g., Jacob et al., 2014, and others). The dynamical downscaling approach is well-established and provides physically and temporally consistent fields. However, it still has significant drawbacks due to the high resource demands required for its execution that limit its application, e.g. to deterministic runs instead of (or limited to small) ensemble runs.

On the other hand, statistical downscaling uses coarse data from numerical simulations to infer data at high resolution by applying empirical relationships or transfer functions derived from a set of known predictors–predictands data pairs (Maraun and Widmann, 2018). Statistical downscaling methods have evolved over the years since the 1990s, with increasingly greater levels of complexity and data. Canonical examples of statistical downscaling methods are linear or multilinear regression methods (e.g., von Storch et al., 1993; Sharifi et al., 2019), analog ensemble downscaling (e.g., Sperati et al., 2024) or quantile mapping (Panofsky and Brier, 1968).

In recent years, the advent of machine-learning techniques introduced many other powerful methods. These approaches have the potential to outperform classical statistical models, introducing nonlinear components in the downscaling process and learning from the provided high-resolution data. Specifically, Convolutional Neural Networks (CNNs) are particularly well suited for handling spatially distributed data and for the super-resolution task, being able to capture complex, nonlinear mappings identifying crucial features, and have already been successfully applied to weather downscaling (e.g., Baño Medina et al., 2020; Rampal et al., 2022; Höhlelein et al., 2020). Building on CNN frameworks, two Deep Learning (DL) approaches are currently the most promising for improving atmospheric downscaling: Generative Adversarial Networks (GANs, Goodfellow et al. (2014, 2020)) and Diffusion Models (Sohl-Dickstein et al., 2015), which both allow for a probabilistic approach to the problem. The potential and drawbacks of these approaches are reported in the following Section 2.

In this work, we focus on and test a Latent Diffusion Model (LDM) that is novel for application to the atmospheric downscaling task. Its advantages should be twofold: the diffusion approach has a much more stable training than that of GAN models, still holding the ability to generate small-scale features and the potential for ensemble production, and shows superior results in applications to image processing compared to GANs (Saharia et al., 2023; Dhariwal and Nichol, 2021). In addition, the latent approach should be seen as incremental compared to pixel-space-based diffusion approaches as it provides a cheaper solution in terms of computational costs for both inference and training (Rombach et al., 2021). This feature is intrinsically appealing to scale the downscaling task to wider (and longer) domains. Lastly, we use the high-resolution output from a numerical model dynamical downscaling simulation as our target-reference-truth. In doing so, we aim to determine whether a properly trained

deep learning model can effectively emulate dynamical downscaling. If successful, this model could serve as a versatile dynamical downscaling emulator, much faster than the traditional numerical dynamical models, with a broad range of utmost significant applications.

2 Related work and Contribution

As mentioned above, currently, the most promising DL approaches for improving atmospheric downscaling are Generative Adversarial Networks (GANs) and Diffusion Models, which both are based on CNN frameworks, allow for the generation of small-scale features and for a probabilistic approach to the problem. GANs have already shown promising results in downscaling different meteorological variables, in different regions. For example, Leinonen et al. (2021) applied GANs for reconstructing high-resolution precipitation patterns from coarsened radar images; Stengel et al. (2020) demonstrated GANs potential in performing downscaling of GCMs up to 2km for solar radiation and wind; steps forward pure super-resolution applications have also been made with GANs, as shown in Harris et al. (2022) as well as in Price and Rasp (2022), where additional variables from numerical models are used as input predictors variables to produce high-resolution precipitation fields. Nevertheless, GANs still pose relevant challenges, such as model instabilities, and mode collapses during the training procedure (Arjovsky and Bottou, 2017; Mescheder et al., 2018).

On the other hand, Diffusion models introduce a relatively younger approach but have already been proven very effective in weather forecasting and nowcasting applications (e.g., Leinonen et al., 2023; Li et al., 2024). Diffusion models have yet to be widely tested and evaluated on the atmospheric downscaling task, but their characteristics and capabilities are undoubtedly promising for this application as shown for example in Addison et al. (2022) and Mardani et al. (2023).

Building on these encouraging results, in this work, we approach the downscaling task with a Latent diffusion model, comparing it against some standard baselines and a GAN baseline. Specifically, we re-adapted the Latent Diffusion Cast (LDCast) model (Leinonen et al., 2023), recently developed for precipitation nowcasting. LDCast has shown superior performance in the generation of highly realistic precipitation forecast ensembles, and in the representation of uncertainty, compared to traditional GAN-based methods. Our resulting model for downscaling, similar to fully convolutional models, can be trained on examples of smaller spatial domains (patches) and used at the evaluation stage on domains of arbitrary sizes, making it suitable for the generation of high-resolution data covering wider domains. As also suggested in Mardani et al. (2023), we propose the application of the diffusion model with a residual approach, relying on a standard UNET architecture for capturing the bigger scales and training the latent diffusion model to generate the residual, small scales only.

Additionally, our work differs from most of the aforementioned works for the chosen pair of low-resolution and high-resolution data for the training. This choice highly influences the level of complexity that the DL downscaling model must achieve. Indeed, downscaling a coarsening of the high-resolution data (e.g., Leinonen et al., 2021; Stengel et al., 2020; Vandal et al., 2017) is a much easier task than downscaling modeled low-resolution data (e.g. short-term forecasts as in Harris et al. (2022), seasonal predictions, or climate projections) to independent high-resolution data, either coming from observations or numerical model simulation. While the first exercise falls into a purely super-resolution task, the latter includes learning

potential large-scale model biases and correcting them, or detecting and generating local phenomena that cannot be resolved at the coarse resolution of the large-scale models. In our work, we focus on reanalyses products and we train our models using a set of 14 ERA5 variables as low-resolution input and high-resolution data from a dynamical downscaling of ERA5 (run with the COSMO_CLM model) as target data (2-m temperature and 10-m wind speed horizontal components). This approach is similar to that followed, for example, by Wang et al. (2021) and Mardani et al. (2023). In doing so, we intentionally force the model to learn to generate the effects of those local phenomena resolved by the dynamical numerical model, emulating its behavior.

3 Datasets

3.1 Low- and High-resolution data

The goal of this experiment is to train a DL model to mimic a dynamical downscaling performed with a convection-permitting Regional Climate Model (RCM). The target high-resolution data consists of the hourly Italian Very High-Resolution Reanalyses produced with COSMO5.0_CLM9 (VHR-REA CCLM) by dynamically downscaling ERA5 reanalyses (Hersbach et al., 2020) from their native resolution (25km) up to 2.2km over Italy (Raffa et al., 2021; Adinolfi et al., 2023). Consistently with these target numerical simulations, the input low-resolution data fed to our DL model are ERA5 data.

3.2 Data alignment and preprocessing

ERA5 data have a resolution of 0.25° worldwide, which roughly corresponds to 22 km at the latitudes of the focus domain, while VHR-REA CCLM data have a native resolution of 0.02° (2.2 km). Data from both datasets were preprocessed to re-project, trim, and align the low and high-resolution fields. Specifically, the coordinate reference system (CRS) chosen for the experiment is ETRS89-LAEA Europe (Lambert Azimuthal Equal Area), also known in the EPSG Geodetic Parameter Dataset under the identifier EPSG:3035, and the experiment grids align with the European Environmental Agency Reference grid (EEA Reference grid, Peifer (2018)). ERA5 was reprojected and interpolated (with nearest-neighbor interpolation) on the EEA 16-km reference grid while VHR-REA CCLM was reprojected and interpolated on the EEA 2-km reference grid. The factor of the downscaling procedure is, therefore, 8x: over the target domain, low-resolution data consists of 72×86 16-km pixel images while high-resolution data consists of 576×672 2-km pixel images.

3.3 Experimental domain

The experiment target domain spans from 35°N to 48°N , and from 5°E to 20°E (Figure 1). This area corresponds to the region where VHR-REA CCLM data are available. The region includes a wide variety of topographically different sub-areas (mountainous areas such as the Alps and the Appennini, flat areas such as the Po Valley and coastal lines) which trigger local phenomena whose effects are challenging to identify for the downscaling models, as they are not present in the low-resolution data.

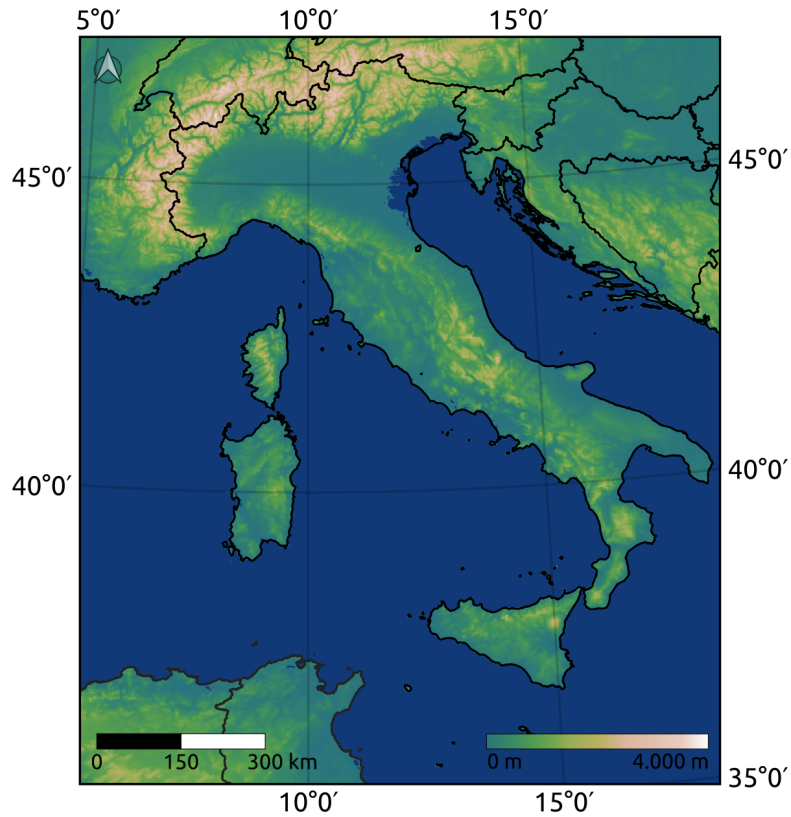


Figure 1. Experimental domain with 2-km digital elevation model.

3.4 Target variables and predictors

The target variables of the study are (i) 2-m temperature and (ii) horizontal wind components at 10 m: different, dedicated models to each target variable have been trained. The input ERA5 low-resolution data are both the target variables and additional fields used as dynamical predictors, to improve models' performance. The choice of the set of input fields was based on previous literature (e.g., Höhle et al., 2020; Rampal et al., 2022; Harris et al., 2022) and on hardware constraints for the experiment. The selected fields used as predictor variables, for both target variables, are the following, corresponding to a total of 14 input channels to our networks:

- 2-m temperature
- 10-m zonal and meridional wind speed
- mean sea level pressure

- sea surface temperature
- snow depth
- dew-point 2-m temperature
- incoming surface solar radiation
- temperature at 850 hPa
- zonal, meridional and vertical wind speed at 850hPa
- specific humidity at 850 hPa
- total precipitation

In addition, high-resolution static data have been fed to the models to guide the training and improve performance. These fields include:

- Digital Elevation Model (DEM)
- land cover categories
- latitude

DEM data consists of the Copernicus Digital Elevation Model (DEM, Copernicus (2023)) interpolated from a resolution of 90 m to a resolution of 2 km. Land cover data were retrieved from the Copernicus Land Service, Global Land Cover data (GLC, Buchhorn et al. (2020)) interpolated from a resolution of 100 m to a resolution of 2 km. Given that land cover was utilized as a static variable in our analysis, we selected data from 2015: this year represents the earliest epoch available for the selected GLC dataset and falls approximately amid our experimental period of 2000-2020. Land cover class data have been converted to single-channel class masks for the DL models (totaling 16 channels). All static fields have been re-projected and aligned to the high-resolution 2-km EAA reference grid.

3.5 Dataset splitting strategy

The experiment database comprises hourly data from 2000 to 2020 (184000 timestamps), for both low and high-resolution data. 70% of data were used for training, 15% for validation and 5% for testing (corresponding to 15, 3 and 1 year, respectively). The testing dataset was fixed to 1 year (5% of the dataset) because of time constraints in running all the models for the evaluation, especially the diffusion model.

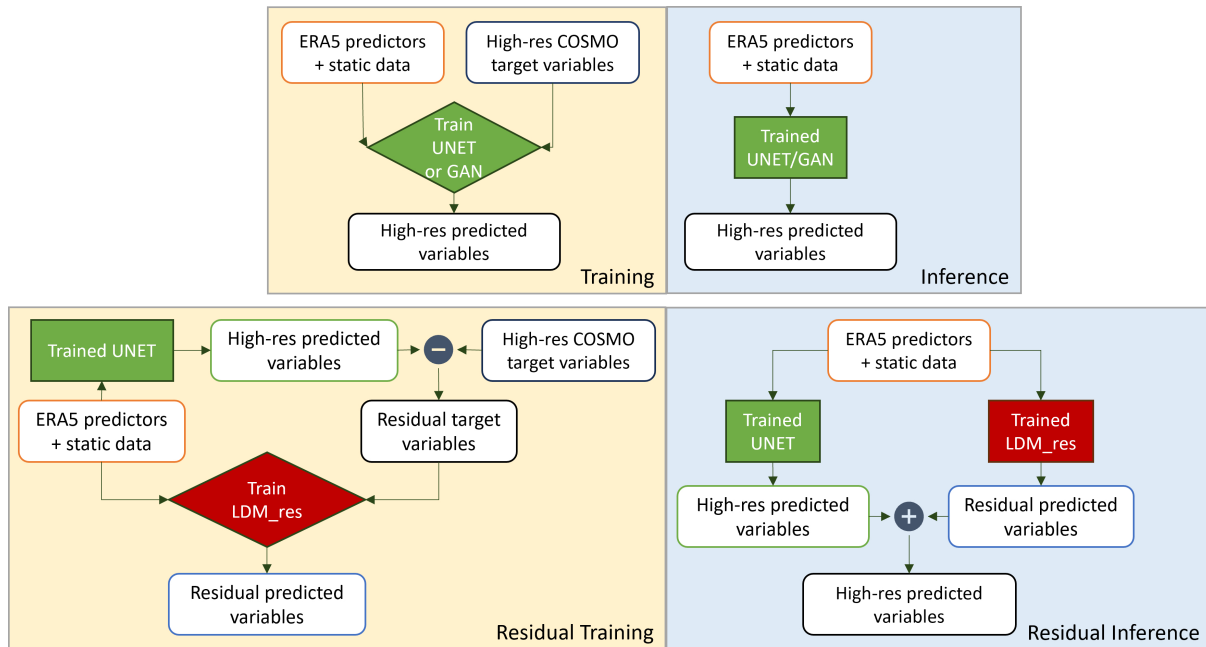


Figure 2. Training and Inference flowcharts for the UNET and GAN models (top row) and for LDM_res (bottom row): differences between the non-residual and residual approaches are highlighted.

4 Methods

In this work, we test a deep generative Latent Diffusion Model (LDM) for the downscaling task, conditioned with low-resolution predictors and high-resolution static data. The implemented LDM is trained to predict the residual error between a previously trained reference UNET and the target variables, hence the model will be addressed as LDM_res (LDM_residual) hereafter. This residual approach has shown great performance in the application of pixel-space diffusion models (Mardani et al., 2023) and is tested here in the latent diffusion context. The underlying idea is to exploit the great ability of a relatively simple network (a UNET) to properly capture the main, bigger-scale variability of the atmospheric high-resolution data and leverage the power of the generative diffusion model to only focus on the reconstruction of the smaller-scale, locally-driven variability of the fields. Figure 2 shows the high-level flow chart of the training and inference setup for LDM_res, while Section 4.3 holds the detailed description of LDM_res architecture.

LDM_res is compared against three different baselines with increasing levels of complexity: the quadratic interpolation of ERA5, a UNET, and a Generative Adversarial Network (GAN). The implemented UNET is the core base for each tested deep-learning architecture. Indeed, the same reference UNET network is used (i) as a baseline, (ii) as the Generator of the implemented GAN, and (iii) for the calculation of the residual on which LDM_res is trained. With this approach, we aim to fairly compare the power of generating small-scale features of the adversarial and the diffusion methods.

Table 1. Number of trainable parameters for each tested model.

Model	Sub-net	# of trainable parameters	
		per subnet	total
UNET		~31M	~31M
GAN	UNET-Generator	~31M	~34M
	Discriminator	~3M	
LDM	VAE	~115K (2mT), ~430K (UV)	
	Conditioner	~24M	~300M
	Denoiser	~275M	

A dedicated network has been trained for each model type, for the two target variables: the 2-m temperature and 10-m horizontal wind components. The downscaling is performed for fixed time steps, with an image-to-image approach.

Given the incremental complexity of the tested models, in the following sections, we start by describing the core reference UNET architecture (Section 4.1), then the GAN architecture (Section 4.2), and finally LDM_res architecture (Section 4.3). Table 1 shows the number of trainable parameters for each model.

4.1 UNET Architecture

The core UNET network implemented for our experiments is a standard UNET architecture (Ronneberger et al., 2015), featuring an encoder (contracting path), a bottleneck, and a decoder (expansive path), with skip connections bridging corresponding levels between the encoder and decoder to preserve spatial information. To use a standard UNET to perform downscaling, the input low-resolution data are interpolated with the nearest neighbor interpolation to the target high resolution before feeding them to the network. The encoder is composed of four blocks, each consisting of a layer containing two consecutive 2D convolutions with ReLU activation, interspersed with batch normalization to ensure stable learning (Ioffe and Szegedy, 2015), and a max-pooling operation. The max-pooling layer reduces the spatial resolution by half, enabling the model to capture increasingly complex features while reducing the image dimensions. The output of each encoder block is used in both the next encoder block and the corresponding decoder block through skip connections. The decoder mirrors the encoder with transposed 2D convolutional layers and upsampling steps to go back to the starting resolution. The use of batch normalization ensures robust learning, while the skip connections help preserve critical spatial information across the encoder-decoder bridge. The total number of trainable parameters for the UNET is ~31 M (Table 1). Details on the UNET structure and resolutions are depicted in Figure 3.

4.2 GAN Architecture

The Generative Adversarial Network (GAN) (Goodfellow et al., 2014, 2020) tested in this experiment consists of deep, fully convolutional Generator and Discriminator networks, conditioned with low-resolution predictors and high-resolution static

data. The generator is trained to output fields that cannot be distinguished from ground truth images by a discriminator, which is trained on the other hand to detect the generator’s ‘fake’ outputs. Our reference GAN consists of a UNET generator upgraded with a Patch-GAN discriminator (Isola et al., 2017). The input data to the generator are low-resolution predictors and high-resolution static data only (no noise addition is performed) and we, therefore, obtain a deterministic GAN.

The generator architecture consists exactly of the UNET described in Section 4.1, as shown in Figure 3.

The discriminator is a PatchGAN convolutional classifier (Isola et al., 2017), which focuses on structures at the scale of image patches. The structure of the discriminator is composed of modules of the form convolution-BatchNorm-ReLu. It assigns a "realness" score to each $N \times N$ patch of the image, runs convolutionally across the image, and allows us to obtain an overall score by averaging all responses for each patch. High-quality results can be obtained with patches much smaller than the full size of the image, with relevant advantages in terms of resources for the training and application to arbitrarily large images. Details on the discriminator network structure and resolutions are depicted in Figure 3. The total number of trainable parameters for the GAN is ~ 34 M (Table 1).

The training procedure follows the combined loss function approach for GANs (Goodfellow et al., 2020), including recent improvements to promote stability in the training (Esser et al., 2021), with the primary goal of balancing the minimization of both the generator’s and discriminator’s losses, which are adversarial. The pixel loss we used is the mean absolute error, while the discriminator loss is the hinge loss. The discriminator is activated after 50000 training steps, giving the generator time to learn to generate consistent outputs and thus stabilizing the adversarial training (Esser et al., 2021). After activating the discriminator, the network is trained by updating alternatively the gradients of the generator and the discriminator. The network is constantly fed with the whole target domain and no patch-training is applied.

4.3 Latent Diffusion Model Architecture

Diffusion Models (Sohl-Dickstein et al., 2015) are probabilistic models meant to extrapolate a data distribution $p(x)$ by corrupting the training data through the successive addition of Gaussian noise (fixed) and then learning to recover the data by reversing this noising process (generative).

The Latent Diffusion Model (LDM) applied for this experiment is an architecture derived from Stable Diffusion (Rombach et al., 2021), specifically a re-adaptation of the conditional LDM LDCast (Leinonen et al., 2023), developed for precipitation nowcasting and already successfully applied for other variables (e.g., Carpentieri et al., 2023). The latent diffusion model derived for the downscaling task is composed of three main elements: (i) a convolutional Variational AutoEncoder (VAE), used to project the residual high-resolution target variables to and from a latent space; (ii) a conditioner, used to embed low-resolution data and high-resolution static data; and a denoiser, used to manage the diffusion process within the latent space. In the following sections, we report a detailed description of each model component. The total number of trainable parameters is shown in Table 1, while Figures 4 and 5 summarize the training and inference procedures for the model and the main structure of each component architecture, respectively.

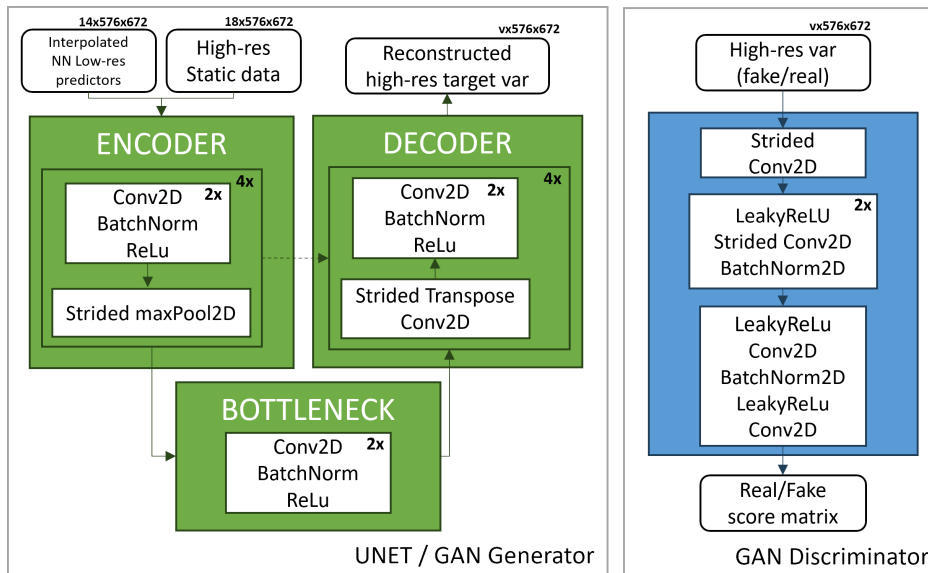


Figure 3. Details on the architectures for the reference UNET and the GAN implemented for the downscaling task. The reference UNET and the generator networks are depicted on the left panel, and the discriminator network is on the right panel. *NN* stands for Nearest Neighbor.

4.3.1 Variational Autoencoder

The Variational Autoencoder (VAE) projects the residual high-resolution data from the pixel space to a continuous latent space (encoder) and projects them back to the pixel space (decoder). We train a dedicated VAE for the 2-m temperature and a dedicated VAE for the 10-m wind speed components, independently from the conditioner and denoiser. Once trained, the VAE weights are kept constant during the training of the rest of the network architecture. During inference, only the decoder of the VAE is used (see Figure 5).

The encoder and the decoder are structured as 2D convolutional networks composed of blocks of a ResNet residual block (Stephan et al., 2008) and a downsampling/upsampling convolutional layer. Three levels of such blocks are used, each reducing each spatial dimension by a factor of 2, while the number of channels is bottlenecked at 32 times the number of input target variables (i.e. 32×1 for the 2-m temperature and 32×2 for the 10-m wind speed components). The VAE bottleneck latent space is regularised with a loss based on Kullback-Leibler divergence (KL) (Kullback and Leibler, 1951; Csiszar, 1975) between the latent variable and a multivariate standard normal variable.

While the space dimensions are reduced by a factor of 8^2 (from 512×512 to 64×64 pixel patches), the number of channels is increased from 1 (for the 2-m temperature) and 2 (for the 10-m wind speed components) to 32 and 64, respectively: the overall amount of data is therefore compressed only by a factor of 2, for both the VAEs (from $1 \times 512 \times 512$ to $32 \times 64 \times 64$ and from $2 \times 512 \times 512$ to $64 \times 64 \times 64$). Nevertheless, the gain in training performance of the denoiser and conditioner is much greater

than the data reduction factor as the compression along the space dimension is more relevant for reducing the computational cost of the training than the increase in channel number (Rombach et al., 2021).

Figure 4 depicts details of the VAE’s structure.

4.3.2 Conditioner

The conditioner stack acts as a context encoder to process the low-resolution predictors and high-resolution static data and embed them into each level of the denoiser UNET architecture. Initially, both datasets are preprocessed by passing through a dedicated encoder, a projection layer, and an analysis sequence, before being merged. The predictors’ encoder is a basic Identity layer as they already have the same spatial dimensions as the latent space (64x64). The static data encoder is a variational encoder with the same structure as the VAE described in the previous Section 4.3.1. For both datasets, the projection layer is a 2D convolutional layer with unitary kernel size, used to increase the number of channels, and the analysis is a sequence of 4 2D Adaptive Fourier Neural Operator (AFNO) blocks (following Pathak et al. (2022)), used to extract relevant features. After pre-processing, the conditioning information is prepared to be fed into each level of the denoiser UNET by applying a combination of average pooling and 2D Resnet layers. Figure 4 depicts details of the conditioner’s structure.

4.3.3 Denoiser

Our denoising stack is structured as the one of the LDCast (Leinonen et al., 2023), a re-adaptation of the U-Net-type network applied in the original latent diffusion model (Rombach et al., 2021). The resulting denoiser network consists of a UNET backbone enabled with a conditioning mechanism based on 2D AFNO blocks (Leinonen et al., 2023), aiming at a cross-attention-like operation (as suggested in Guibas et al. (2022)). This structure is meant to control the high-resolution synthesis process feeding the conditioning in each level of the UNET architecture.

For the downscaling task, the conditioning information consists of the low-resolution predictors’ data and the high-resolution static data, elaborated by the conditioner. Figure 4 depicts details of the denoiser’s structure.

To improve the reconstruction of extreme values (for both temperature and wind speed) we implemented the v-prediction parameterization in our LDM model, following Salimans and Ho (2022): this parameterization trains the denoiser to model a weighted combination of both the noise and the start image, instead of either the only noise or the only start image as done in the more traditional implementations *eps* and *x0*, respectively.

As shown in Figure 5, the conditioner and the denoiser are trained together, minimizing the mean square error (L2), and feeding the network with random patches of ERA5 predictors (64x64 pixels) and static data (512x512 pixels) for the conditioning, and high-resolution target variables (512x512 pixels) for the ground truth. The training is performed using the AdamW optimizer (Loshchilov and Hutter, 2019), and Exponential Moving Averaging (EMA) is applied to the network weights, following Rombach et al. (2021).

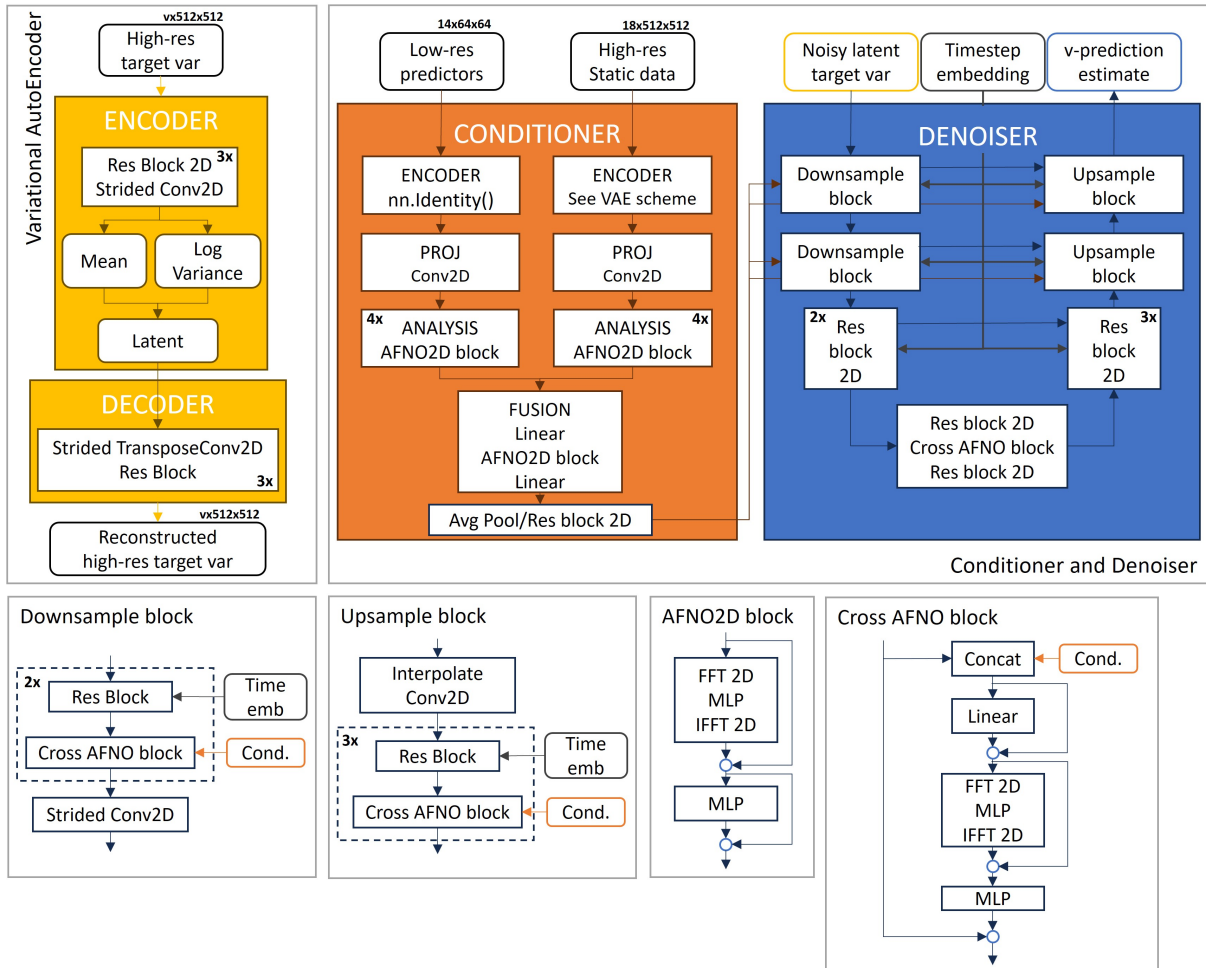


Figure 4. An overview of the components of our downscaling latent diffusion model: the Variational AutoEncoder, the Conditioner, and the Denoiser networks. *Conv* denotes convolution. *MLP* (multilayer perceptron) is a block consisting of a linear layer, activation function and another linear layer. *Res block* denotes a ResNet-type residual block. *v* in the array size labels stands for the number of target variables (1 for 2-m temperature and 2 for 10-m horizontal wind speed components).

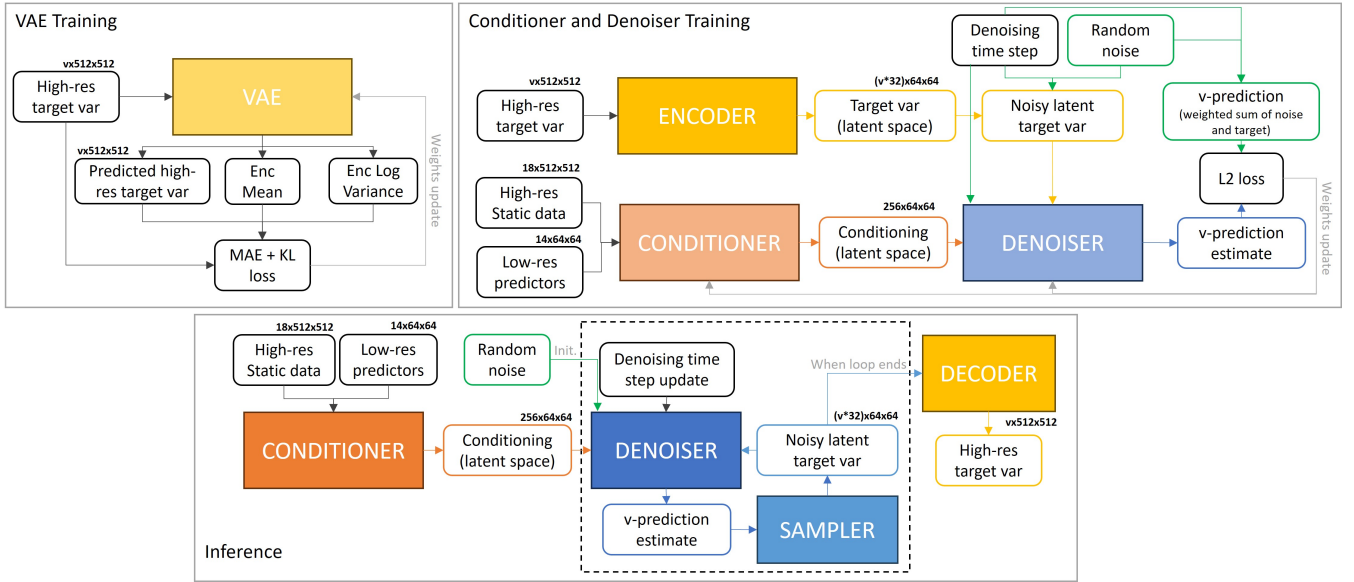


Figure 5. An overview of the training and inference procedures for our downscaling latent diffusion model. v in the array size labels stands for the number of target variables (1 for 2-m temperature and 2 for 10-m horizontal wind speed components).

5 Results

All the presented models were tested on a one-year dataset, which was held out during the training and validation processes. The results from the LDM_{res} are evaluated based on a single inference run, obtained using 100 denoising steps; its potential to produce ensemble results is postponed to future analyses.

The following sections compare the results from LDM_{res} against the baselines using various verification metrics and distributions. In the Supporting Information we report the comparison of results from the LDM trained with and without the residual approach to provide an overview of the improvements introduced by this method.

5.1 Qualitative evaluation

To provide a qualitative and perceptual overview of the obtained results, we present a random snapshot of downscaled variables compared with both the input ERA5 low-resolution data and the COSMO_CLM high-resolution reference-truth (Figure 6). The second and third columns show a zoom-in on Sardinia Island, providing a deeper overview of models' performance over complex terrain, coastal shores, and open sea. Both generative models, the GAN and LDM_{res}, effectively overcome the blurriness observed in both the quadratic interpolation and the UNET for the target variables. Particularly for 2-m temperatures, LDM_{res} demonstrates a remarkable ability to identify and reconstruct discontinuities in the variable field (zoomed-in view in Figure 6). Figure 6 also includes results for 10-meter wind speed (in color), which is a derived field obtained by combining the two actual target variables of the models, U and V. Perceptually, the results for this variable from both the GAN and LDM_{res}

appear similar and equally plausible, displaying significantly more small-scale features compared to the UNET. A deeper qualitative examination reveals that the GAN aligns well with the reference truth, particularly over land, but exhibits mode collapse over the sea for both target variables. An example of this effect is shown in the Supporting Information. Conversely, the LDM_res consistently generates plausible high-resolution data across the entire domain, over both land and sea, and for both target variables.

5.2 Verification deterministic metrics

Figure 7 compares model results for different deterministic metrics, averaging results over the whole domain for each test timestep. In addition to results from the baseline and tested models, Figure 7 also reports results for the VAE of the LDM. These results are obtained using the VAE offline, feeding it with COSMO_CLM high-resolution data and calculating the metrics on the reconstructed data: this allows quantifying the LDM error resulting from the data decompression from the latent space only. We present three distance metrics, the Root Mean Square Error (RMSE), the mean bias (BIAS), and the coefficient of determination (R^2), and one correlation metric, the Pearson Correlation Coefficient (PCC) (all calculated following Bell et al. (2021)).

The UNET and GAN models show comparable and best results for all metrics, except for the bias. Indeed, minimizing the MSE is the exact goal of their training procedure. Conversely, the LDM has been trained on a much different objective but performs very well for all the metrics. As expected, all models struggle more in downscaling the wind components than the 2-m temperature. Biases show that all models perform very well, with LDM_res excelling, especially for temperature. The UNET and the GAN show spatially averaged biases within 1°C for temperature, while LDM_res shrinks this variability to less than 0.5°C . Spatially averaged biases amount to 1 m/s for wind speed, with a narrower spread for LDM_res. The UNET and LDM_res show a less skewed distribution than the GAN model for the 2-m temperature: while the GAN model tends to underestimate the average 2-m temperature mostly, LDM_res shows a very balanced distribution for over- and under-estimations. As for the wind speed biases, all the models always slightly underestimate the target variable.

The results show that the VAE contribution to LDM_res is the highest for the RMSE of 2-m temperature, while bias, R^2 , and PCC have very little to no effects on temperature and wind speed.

5.3 Spatial distribution of errors

The spatial distribution of averaged-in-time magnitude differences for both the target variables and all tested models is illustrated in Figure 8. Within each panel, the numbers in squared brackets represent the 0.5 and 99.5 percentile values, offering insight into the highest errors recorded over the domain. Negative and positive values signify underestimation and overestimation, respectively, for both variables. Results from the quadratic interpolation of ERA5 data provide information on the original input data: 2-m temperature tends to be highly overestimated over complex terrain but underestimated on flat terrain, with smaller errors over the sea. Wind speed, conversely, is largely underestimated over land, particularly over mountain ridges, with a tendency towards overestimation along coastal shores.

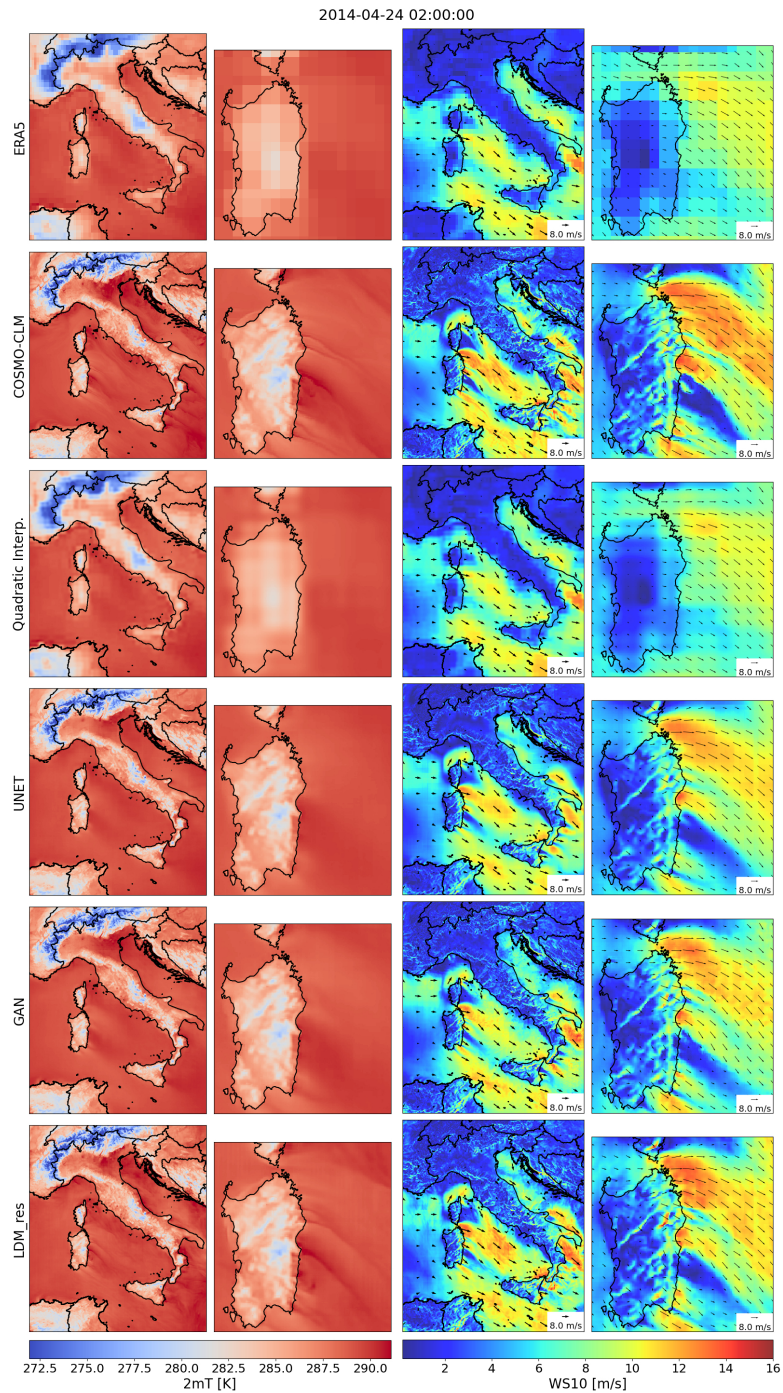


Figure 6. Downscaled variables from all the tested models against low-resolution ERA5 input data and high-resolution COSMO_CLM reference truth, for a randomly picked timestamp. The left columns refer to 2-m temperature, and the right columns refer to 10-m wind speed. The second and fourth columns show a zoom-in on Sardinia Island.

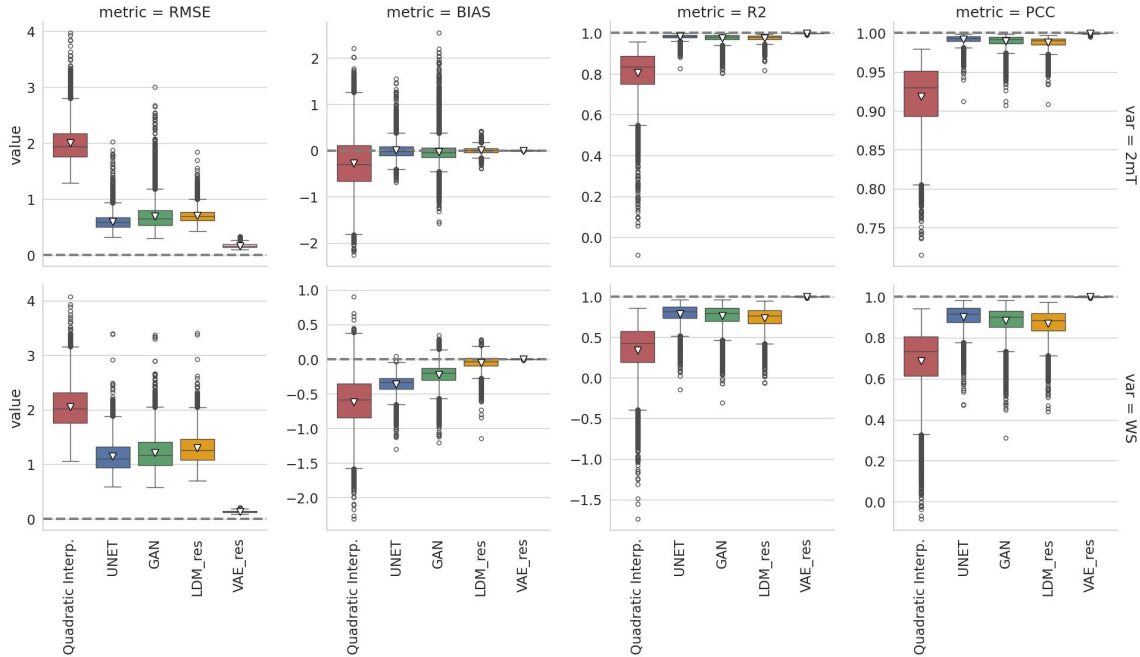


Figure 7. Comparison of deterministic metrics for spatially-averaged results of the analyzed models (top row refers to the 2-m temperature and bottom row refers to the 10-m wind speed). Notice that y axes are not shared between panels. The dashed line highlights the reference value for each metric, and the white triangle highlights the mean metric value.

On the contrary, all DL-based models, including the UNET baseline, exhibit substantially smaller errors. For 2-m temperature, errors remain below 0.3°C , while for wind speed, they stay under 0.8 m/s across the entire domain. Notably, the UNET and GAN models perform comparably well for 2-m temperature, whereas LDM_res excels, leveraging diffusion processes to reduce the UNET errors homogeneously.

As for the wind speed results, all models exhibit a tendency to underestimation. LDM_res demonstrates superior performance, minimizing errors to nearly zero over most of the domain, with a uniform distribution over land and sea. The GAN displays traces of its characteristic mode collapses, especially over the sea: this evidence indicates that these mode collapses persist statically in fixed locations over time, consistently with the deployed training approach (i.e. feeding the network always the entire, fixed domain).

5.4 Frequency distributions

Figure 9 presents the results in terms of frequency distributions. LDM_res precisely captures the reconstruction of the 2-m temperature frequency distribution, surpassing all other models. All DL models effectively mitigate the occurrence of cold extremes evident in the low-resolution data (as demonstrated by the quadratic interpolation distribution) while increasing the incidence of warm extremes. Notably, the adversarial training of the UNET yields marginal enhancements in capturing the

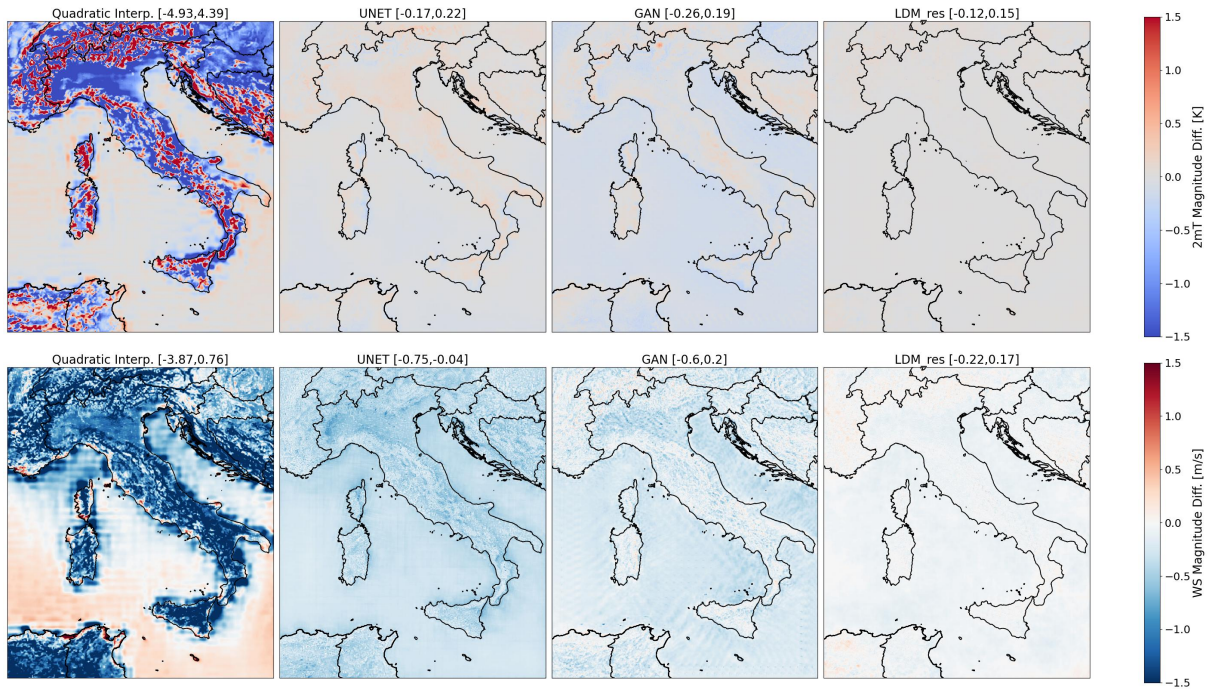


Figure 8. Spatial distribution of averaged-in-time magnitude difference for each tested model. The top row refers to the 2-m temperature, and the bottom row refers to the 10-m wind speed.

frequency distribution, with the GAN slightly outperforming the UNET, particularly regarding cold extremes. Conversely, the diffusion process performed by LDM_res significantly corrects the UNET residual errors, aligning closely with the reference-truth distribution across all temperature values.

Reconstructing the distribution of 10-m wind speed proves more challenging for all models, given the inherent chaotic nature of the U and V wind components compared to temperature, which is strongly influenced by terrain elevation. Nonetheless, performance outcomes mirror those of the 2-m temperature. The GAN modestly improves upon UNET results, primarily in reducing occurrences of low wind speeds. LDM_res exhibits the highest performance in capturing both the tail and center of the wind speed distribution.

5.5 Radially Averaged Power Spectral Density (RAPSD)

Figure 10 showcases the results in terms of Radially Averaged Power Spectral Density (RAPSD), computed following the implementation outlined in Pulkkinen et al. (2019). The top row of the figure illustrates a single RAPSD, representing the average of each RAPSD calculated for every timestamp within the test dataset. To provide insight into the distribution of these values across all timestamps, the distributions of single-time RAPSD for fixed wavelengths are displayed in the bottom rows of Figure 10.

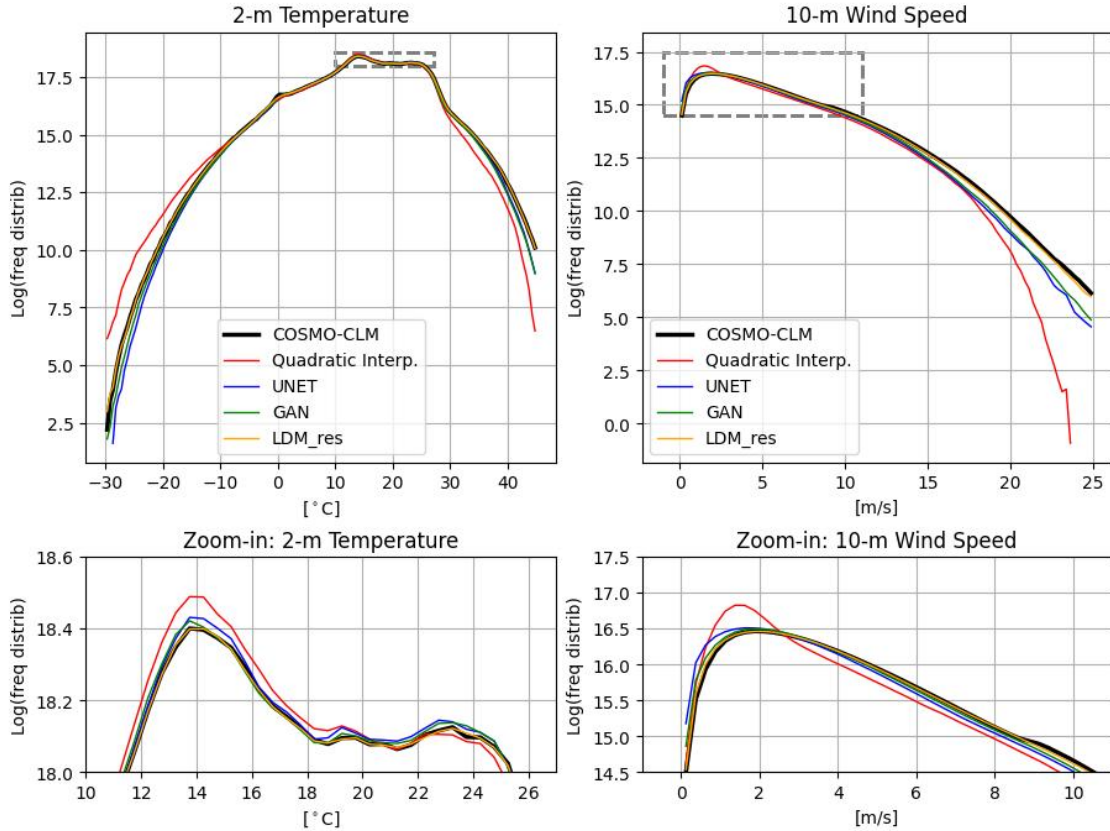


Figure 9. Comparison of frequency distributions for results from the tested models against COSMO-CLM reference-truth. The left column refers to the 2-m temperature, and the right column refers to the 10-m wind speed. Counting of pixel-wise data is cumulated for the yearly test dataset over bins of 0.5 °C and 0.05 m/s for temperature and wind speed, respectively. Notice that y-axes are logarithmic to highlight the tails of the distributions, hence the extreme values. The top row focuses on the tails of the distributions, i.e. on extreme values, while the bottom row focuses on the most frequent values and is a zoom-in on the dashed boxes for each variable.

Overall, all DL models effectively reconstruct the 2-m temperature power spectra down to wavelengths of 10 km. However, LDM_res consistently outperforms both the UNET and the GAN, as evident in panels (b) and (c) of Figure 10. The UNET and the GAN yield similar results, with marginal yet consistent enhancements originating from the adversarial training of the UNET. The diffusion process of LDM_res adeptly enhances the generation of small-scale features, showing precise reconstruction of the spectra up to 9 km (see panel c). For scales smaller than 9-10 km, all models exhibit decreased performance, albeit still showing improvements over the quadratic interpolation of ERA5. LDM_res still outperforms the other models but the very small-scale variability of the original data is slightly underestimated. This behavior is to be ascribed to the VAE, as further elucidated in the Supporting Information. Indeed, original reference-truth data compressed and reconstructed by the

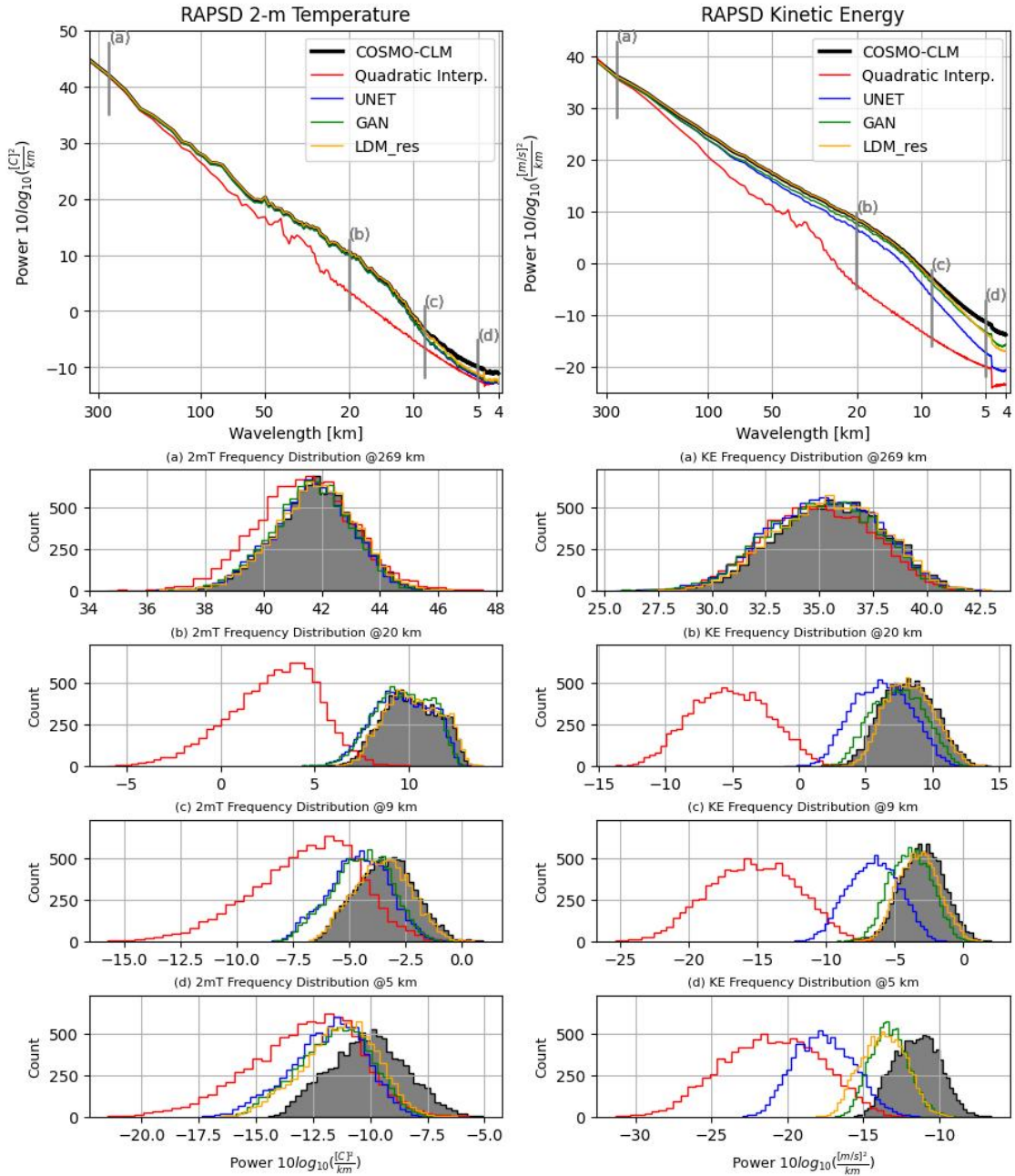


Figure 10. Comparison of Radially Averaged Power Spectral Density (RAPSD) distributions for results from the tested models against COSMO_CLM reference-truth. The left column refers to the 2-m temperature, and the right column refers to the 10-m wind speed. The first row shows the averaged-in-time spectra, across the whole test dataset. Notice that in the first row y-axes are logarithmic to highlight the tail of the distributions, hence the high frequencies. The bottom rows show the distributions of single-time RAPSD values for fixed wavelengths, namely 269, 20, 9, and 5 km.

VAE show the very same power spectra underestimation for scales smaller than 9 km. The loss of information is therefore due to and inherent to the projection to the latent space.

In contrast, results for wind speed distinctly demonstrate that generative models surpass both quadratic interpolation and UNET, effectively matching the slope of the energy power spectra and remaining competitive with each other. Specifically, LDM_res consistently outperforms the GAN up to 7 km, as emphasized in panels (b) and (c) of Figure 10 (right column). Similar to the 2-m temperature, for scales smaller than 10-9 km, both the GAN and LDM_res experience reduced performance, although they consistently exhibit improvements over the UNET. This behavior, for LDM_res, is in this case only partly to be ascribed to the VAE, as further shown in the Supporting Information, and an additional loss, for scales smaller than 9 km, is to be attributed intrinsically to the extraction of features with the diffusion process conditioned with the low-resolution data and high-resolution static data.

5.6 Run-time performance

In this section, we compare the run-time performance of our tested models. These characteristics are of fundamental importance given the potential target applications of such models. Table 2 reports data for each model: to give a whole picture of the needed resources we provide information on both the training and inference requirements. The hour budgets indicated for LDM_res include hours to train/run the UNET, which is needed to provide the residual data, and the VAE_res. LDM_res budgets are therefore comprehensive of the required computational time to train and run the whole modeling chain from scratch. Simulations were run either on NVIDIA GeForce RTX 4090 or NVIDIA A100 GPUs. The training dataset comprises 129000 hourly samples over a target domain of 576x672 pixels (at high resolution) and 72x86 pixels (at low resolution). The UNET and GAN training ran with 4-size batches for both target variables on the whole target domain. LDM_res training ran with 8- and 4-size batches for the two target variables (2-m temperature and 10-m wind components, respectively) on patches of 512x512 and 64x64 for high-resolution and low-resolution data, respectively. Inference times are calculated running with single-dimension batches, on the size of the entire domain.

As shown in Table 2, LDM_res implies more expensive training and inference processes when compared with the tested DL baselines. This evidence is expected, given the more complex structure of the diffusion model and its dimensions in terms of trainable parameters, which is an order of magnitude greater than that of the baselines. Nevertheless, the required computational time for both training and inference remains contained and competitive with the other available options. LDM_res requires 10 days over 8 GPUs to train the models for both the target variables and 30 hours on a single GPU to downscale one year of hourly temperature and wind data. As a term of comparison, we note here that a 1-year-long COSMO_CLM simulation ran over the very same domain requires 61 h, running on 2160 cores (Raffa et al., 2021) (of course producing many more high-resolution variables than the sole 2-m temperature and 10-m horizontal wind components).

Table 2. Number of GPU hours required for the training and inference (of a 1-year-long test set) by each tested model.

Model	Training		Inference	
	2mT	UV	2mT	UV
UNET	~250	~380	~1	~1
GAN	~300	~100	~1	~1
LDM_res	~870	~1100	~15	~16

6 Discussion and Conclusions

This study compares the performance of various downscaling models, focusing on their ability to reconstruct high-resolution meteorological variables from low-resolution input data. The models evaluated include a baseline UNET, a Generative Adversarial Network (GAN), and a Latent Diffusion Model with a residual approach against the reference UNET (LDM_res). The results are analyzed using qualitative evaluations, deterministic metrics, spatial error distributions, frequency distributions, Radially Averaged Power Spectral Density (RAPSD), and runtime performance.

LDM_res demonstrates superior performance across most metrics, particularly in reconstructing fine-scale details and maintaining accuracy in frequency distributions (especially for the extreme values) and spatial error distributions. LDM_res outperforms the other models in reconstructing the power spectra, showing superior performance, especially for wind speed, with outstanding results up to 7 km wavelengths. Residual errors at smaller scales can be attributed to the data projection into the latent space, specifically to the usage of the VAE. This performance loss might be mitigated by conducting the diffusion process directly in the pixel space. However, this alternative approach would substantially increase the computational costs for both training and inference.

The remarkable results of LDM_res are to be ascribed equally to two fundamental aspects of the proposed model:

- the incomparable effectiveness of the diffusion process in extracting features and leveraging the provided conditioning;
- the residual approach which allows the diffusion process to focus only on smaller scales and more subtle characteristics of the fields, delegating the estimates of large-scale variation of the atmospheric fields to a simpler, yet effective, network.

However, the great performance of LDM_res comes at the cost of significantly higher computational requirements for both training and inference, when compared to the other DL models, the UNET or the GAN. Nonetheless, LDM_res still offers a significant advantage in terms of inference speed and computational efficiency once the model is trained when compared to the extensive computational resources required by COSMO_CLM.

In conclusion, the ability of LDM_res to accurately reproduce the statistics of the COSMO_CLM model reference truth data, provided with the same input, demonstrates its potential as an effective and versatile dynamical downscaling emulator. This approach significantly accelerates the downscaling process compared to traditional numerical dynamical models, making it highly suitable for a broad range of important applications, such as downscaling seasonal forecasts or climate projections.

However, a primary limitation of such deep learning models remains the temporal consistency of the generated fields which is not provided by the construction of the models.

7 Future work

The results presented in this work suggest several promising directions for further investigation into the application of latent diffusion models for downscaling. Future research could explore the ensemble generation capabilities of our Latent Diffusion Model, its effectiveness in downscaling discontinuous and chaotic variables such as precipitation, crucial for many applications, and the temporal consistency of the downscaled data, including methods to enforce this consistency within the model architecture. Long-term developments may include applying latent diffusion models to real-time weather forecasts, seasonal forecasts, and climate projections, with adjustments in the training procedure, particularly in selecting low-resolution input predictors and target reference truths.

Code and data availability. Data from ERA5 (Hersbach et al., 2020) was used as input low-resolution data for our models and was downloaded from the Copernicus Climate Change Service (Hersbach et al., 2023a, b). The results contain modified Copernicus Climate Change Service information 2020. Neither the European Commission nor ECMWF is responsible for any use that may be made of the Copernicus information or data it contains. The target high-resolution VHR-REA_IT data (Raffa et al., 2021; Adinolfi et al., 2023) was downloaded from the Euro-Mediterranean Center on Climate Change (CMCC) Data Delivery System (CMCC, 2021). CMCC produced the VHR-REA_IT dataset as a part of the Highlander project and released it under the CC BY 4.0 Licence. The full, preprocessed dataset used for the presented experiments is available on Zenodo (Tomasi et al., 2024c, d, e, f, g, h, i). Additionally, Zenodo hosts a sample dataset (Tomasi et al., 2024a) to test and train the models and the trained models themselves (Tomasi et al., 2024b). A dedicated GitHub repository (<https://github.com/DSIP-FBK/DiffScaler>) hosts the Pytorch Lightning (Falcon and The PyTorch Lightning team, 2019) code of the models described in this paper, based on the Lightning-Hydra-Template (Yadan, 2019), licensed under the MIT License. The repository also hosts the code to reproduce all the images shown in this paper. LDM_res v1.0 GitHub release is archived on Zenodo (Franch et al., 2024) and allows to download the code to reproduce the presented experiments.

Appendix A: Additional snapshots of downscaled data

Some additional snapshots of downscaled data from all the tested models are shown in the following Figures A1 and A2. The left columns refer to 2-m temperature, and the right columns refer to 10-m wind speed. The second and fourth columns show a zoom-in on Sardinia Island.

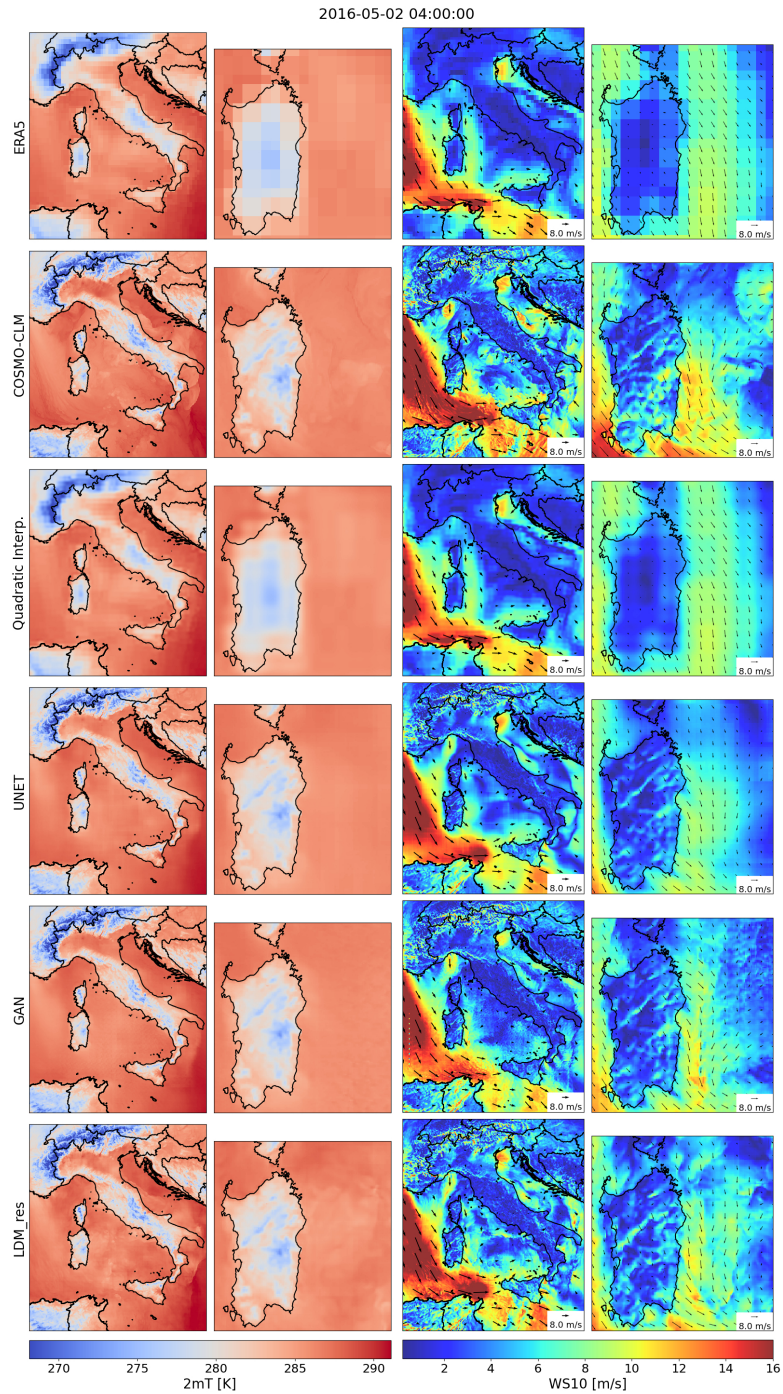


Figure A1. Downscaled variables from all the tested models against low-resolution ERA5 input data and high-resolution COSMO-CLM reference truth, for an additional random timestamp.

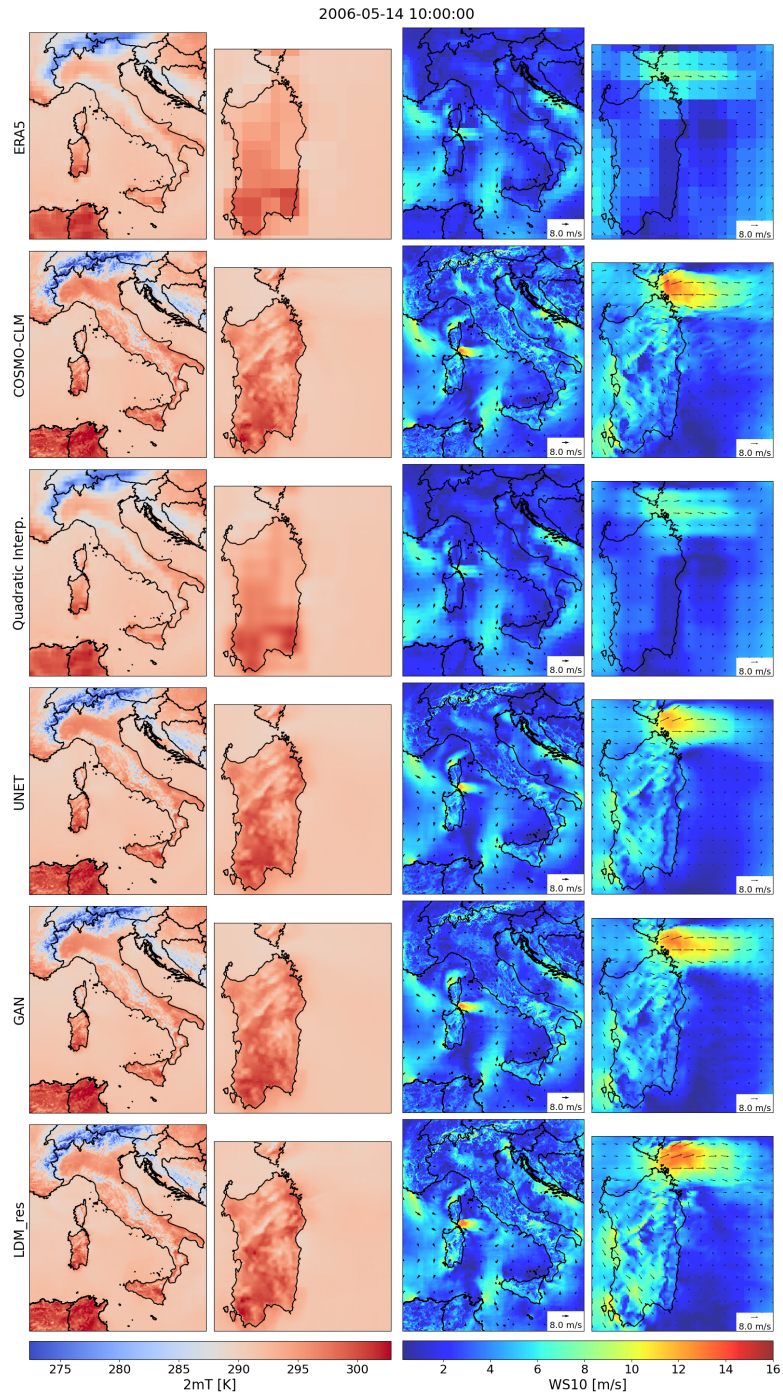


Figure A2. Downscaled variables from all the tested models against low-resolution ERA5 input data and high-resolution COSMO-CLM reference truth, for an additional random timestamp.

Appendix B: Calculation of verification metrics

In Section 5.2, we discuss the following metrics: three distance metrics, the Root Mean Square Error (RMSE), the mean bias (BIAS), the coefficient of determination (R2), and one correlation metric, the Pearson Correlation Coefficient (PCC). All the metrics are calculated with the xskillscore library Bell et al. (2021). Definitions are the following:

$$\text{RMSE} = \sqrt{\frac{1}{n} \sum_{i=1}^n (a_i - b_i)^2} \quad (\text{B1})$$

$$\text{BIAS} = \frac{1}{n} \sum_{i=1}^n (a_i - b_i) \quad (\text{B2})$$

$$SS_{tot} = \sum_{i=1}^n (a_i - \bar{a})^2 \quad (\text{B3})$$

$$SS_{res} = \sum_{i=1}^n (a_i - b_i)^2 \quad (\text{B4})$$

$$R^2 = 1 - \frac{SS_{res}}{SS_{tot}} \quad (\text{B5})$$

$$PCC = \frac{\sum_{i=1}^n (a_i - \bar{a})(b_i - \bar{b})}{\sqrt{\sum_{i=1}^n (a_i - \bar{a})^2} \sqrt{\sum_{i=1}^n (b_i - \bar{b})^2}} \quad (\text{B6})$$

where a and b are the predicted and reference truth values, respectively, for every i^{th} pixel of the domain; n are the total number of pixels in the domain.

Appendix C: On the contribution of the VAE

Figure C1 compares power spectra from the COSMO-CLM test reference truth data with power spectra from high-resolution test data generated using three models: the quadratic interpolation of ERA5 data, VAE_res, and LDM_res. This figure highlights the decompression stage’s contribution from the latent space to the pixel space in LDM_res.

VAE_res takes as input the original reference truth high-resolution target variables. LDM_res takes as input the low-resolution ERA5 predictors, the high-resolution static data, and random noise, produces information in the latent space, and projects them in the pixel space using the VAE Decoder. Both VAE_res and LDM_res also use the corresponding UNET estimates for each target variable, but these quantities are subtracted before the encoding step (when applied) and added back after

the decompression stage, acting essentially as constants. Therefore, the reconstruction errors in the power spectra for VAE_res are thus solely attributed to the compression/decompression processes, while the reconstruction errors in the power spectra for LDM_res arise from both the diffusion and decompression processes.

For 2-m temperature, the power spectra from the VAE_res and LDM_res are nearly identical across all wavelengths, including the smallest scales. This indicates that the errors in reconstructing the spectra with LDM_res are attributable solely to the decompression stage, with the diffusion process effectively and accurately extracting latent features from the conditional data. On the contrary, for 10-m wind speed, a more chaotic field, discrepancies between the power spectra from LDM_res and VAE_res are observed at scales smaller than approximately 7 km. These differences highlight the errors introduced by the sole extraction of features by the diffusion process.

Appendix D: LDM residual versus non-residual results

In this section, we report the comparison of results from the LDM trained with and without the residual approach, to provide an overview of the improvements introduced by this approach. We compare results in terms of frequency distribution and of Radially Averaged Power Spectral Density, shown in Figures D1 and D2.

The graphs show relevant differences in the performance of the two models, especially in: (i) the estimation of the most frequent values of 2-m temperature, (ii) the reconstruction of the whole frequency distribution of the wind speed, (iii) the reconstruction of the 2-m temperature power spectra at small scales, with performances of LDM with no residual approach degrading below the quadratic interpolation of ERA5, and (iv) the reconstruction of the 10-m wind speed power spectra at all scales, with a quasi-constant lag between the two models throughout all wavelengths.

The corresponding VAEs for the two models (VAE and VAE_res) perform the same except for the small scales of the 2-m temperature power spectra (not shown). Thus, the lack of performance of LDM can be attributed to the VAE only for this occasion (i.e., (iii)). All the other listed deficiencies are to be solely attributed to the diffusion process itself, which, when trained to reconstruct a residual field instead of the original target variable field, gains performance in the reconstruction of all the frequency distributions, and of the power spectra across all wavelengths (not only the small scales), especially for chaotic variables such as wind speed.

Author contributions. All authors conceived and conceptualized the study. ET and GF designed the LDM_res architecture and implemented the code for all the tested models. ET managed the data, ran the experiments, performed the analysis and verification of the results, and wrote the manuscript. All authors revised the results and reviewed the manuscript. MC supervised the study from end to end.

Competing interests. The authors declare that they have no conflict of interest.

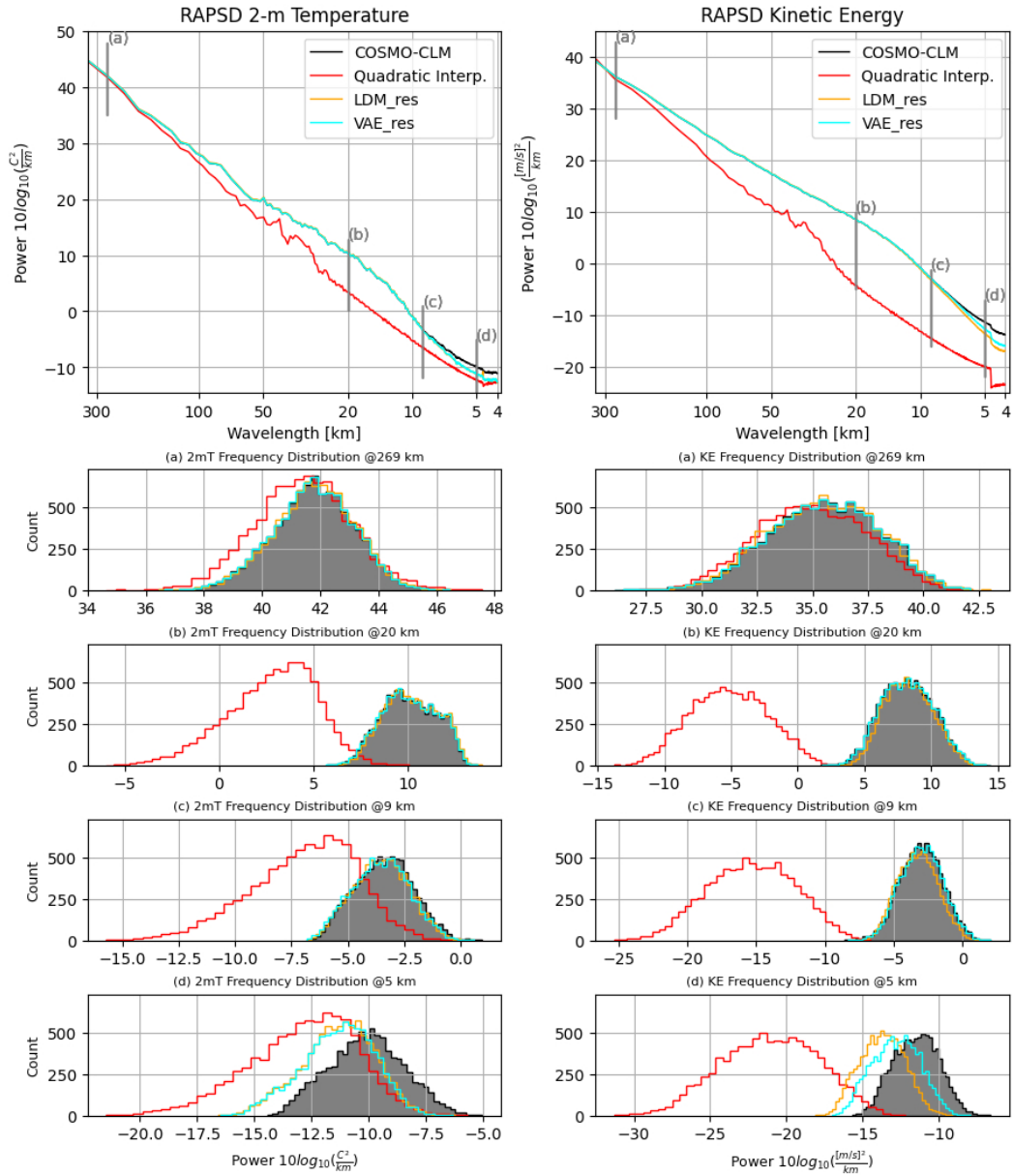


Figure C1. Comparison of Radially Averaged Power Spectral Density (RAPS D) distributions for results from LDM_res and VAE_res against COSMO-CLM reference-truth and ERA5 quadratic interpolation. The left column refers to the 2-m temperature, and the right column refers to the 10-m wind speed. The first row shows the averaged-in-time spectra, across the whole test dataset. Notice that in the first row y-axes are logarithmic to highlight the tail of the distributions, hence the high frequencies. The bottom rows show the distributions of single-time RAPS D values for fixed wavelengths, namely 269, 20, 9, and 5 km.

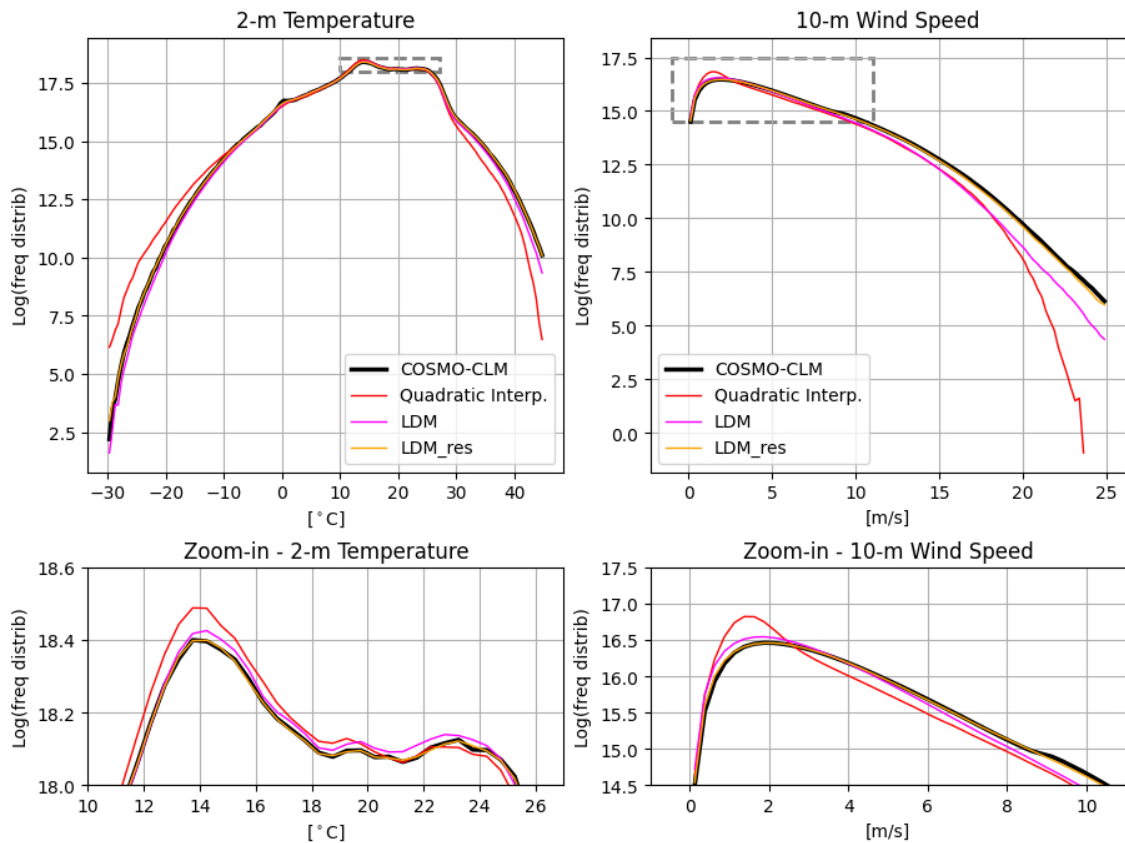


Figure D1. Comparison of frequency distributions for results from LDM and LDM_res against COSMO-CLM reference-truth and ERA5 quadratic interpolation. The left column refers to the 2-m temperature, and the right column refers to the 10-m wind speed. Counting of pixel-wise data is cumulated for the yearly test dataset over bins of 0.5 °C and 0.05 m/s for temperature and wind speed, respectively. Notice that y-axes are logarithmic to highlight the tails of the distributions, hence the extreme values. The top row focuses on the tails of the distributions, i.e. on extreme values, while the bottom row focuses on the most frequent values and is a zoom-in on the dashed boxes for each variable.

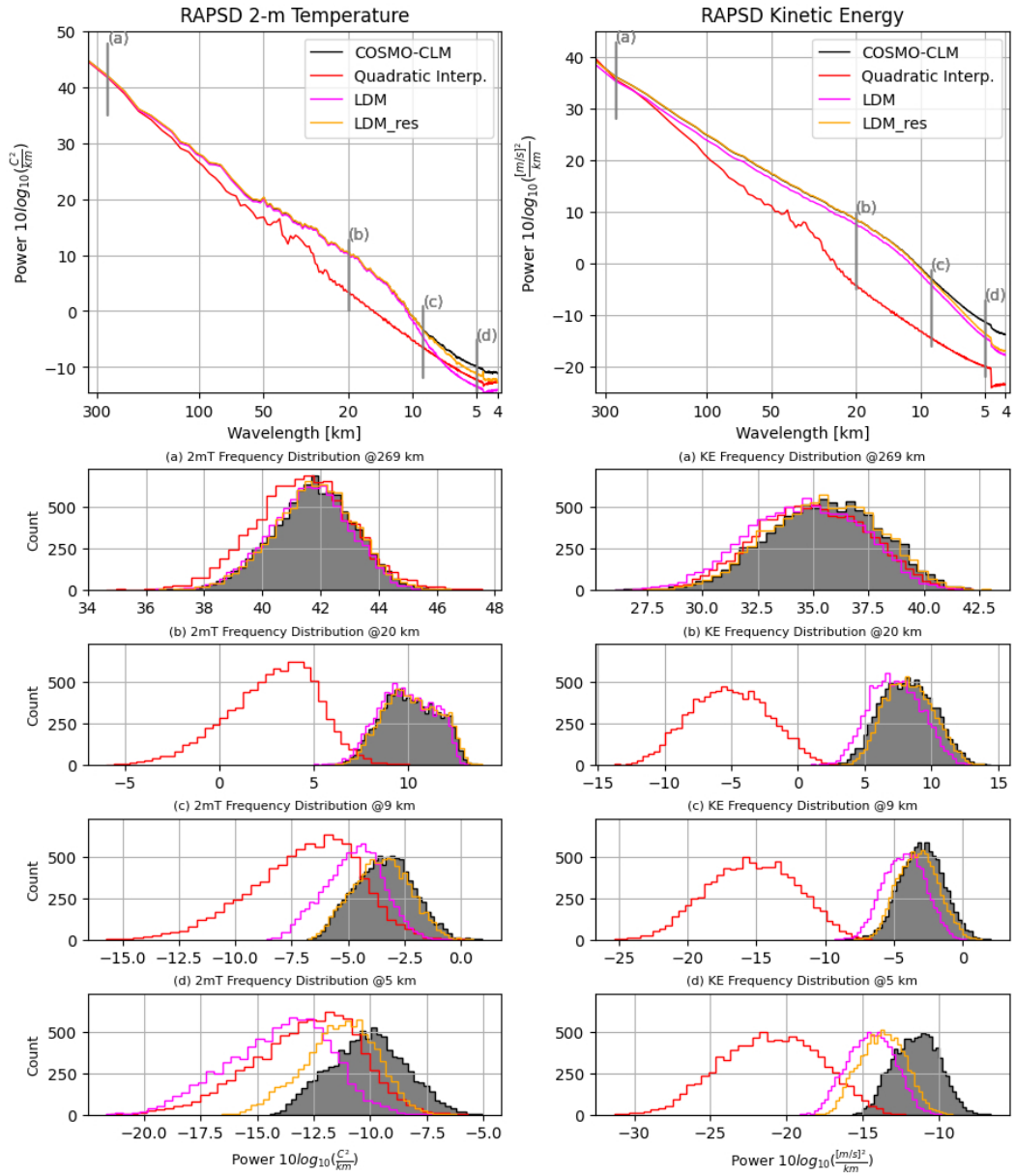


Figure D2. Comparison of Radially Averaged Power Spectral Density (RAPSD) distributions for results from LDM and LDM_res against COSMO-CLM reference-truth and ERA5 quadratic interpolation. The left column refers to the 2-m temperature, and the right column refers to the 10-m wind speed. The first row shows the averaged-in-time spectra, across the whole test dataset. Notice that in the first row y-axes are logarithmic to highlight the tail of the distributions, hence the high frequencies. The bottom rows show the distributions of single-time RAPSD values for fixed wavelengths, namely 269, 20, 9, and 5 km.

Acknowledgements. This work was developed with financial support from ICSC–Centro Nazionale di Ricerca in High Performance Computing, Big Data and Quantum Computing, Spoke4 - Earth and Climate, funded by European Union – NextGenerationEU.

References

- Addison, H., Kendon, E., Ravuri, S., Aitchison, L., and Watson, P. A.: Machine learning emulation of a local-scale UK climate model, 2022.
- Adinolfi, M., Raffa, M., Reder, A., and Mercogliano, P.: Investigation on potential and limitations of ERA5 Reanalysis downscaled on Italy by a convection-permitting model, *Climate Dynamics*, 61, <https://doi.org/10.1007/s00382-023-06803-w>, 2023.
- Arjovsky, M. and Bottou, L.: Towards Principled Methods for Training Generative Adversarial Networks, in: *International Conference on Learning Representations*, https://openreview.net/forum?id=Hk4_qw5xe, 2017.
- ARPAE-SIMC: COSMO ARPAE-SIMC, <http://www.cosmo-model.org/content/tasks/operational/cosmo/arpae-simc/default.htm>, accessed: 20 May 2024.
- Baño Medina, J., Manzanar, R., and Gutiérrez, J. M.: Configuration and intercomparison of deep learning neural models for statistical downscaling, *Geoscientific Model Development*, 13, 2109–2124, <https://doi.org/10.5194/gmd-13-2109-2020>, 2020.
- Baldauf, M., Seifert, A., Förstner, J., Majewski, D., Raschendorfer, M., and Reinhardt, T.: Operational Convective-Scale Numerical Weather Prediction with the COSMO Model: Description and Sensitivities, *Monthly Weather Review*, 139, 3887 – 3905, <https://doi.org/10.1175/MWR-D-10-05013.1>, 2011.
- Bell, R., Spring, A., Brady, R., Andrew, Squire, D., Blackwood, Z., Sitter, M. C., and Chegini, T.: xarray-contrib/xskillscore: Release v0.0.23, <https://doi.org/10.5281/zenodo.5173153>, 2021.
- Buchhorn, M., Smets, B., Bertels, L., De Roo, B., Lesiv, M., Tsendbazar, N. E., Herold, M., and Fritz, S.: Copernicus Global Land Service: Land Cover 100m: collection 3: epoch 2015: Globe (V3.0.1) [Data set], Zenodo, <https://doi.org/https://doi.org/10.5281/zenodo.3939038>, 2020.
- Carpentieri, A., Folini, D., Leinonen, J., and Meyer, A.: Extending intraday solar forecast horizons with deep generative models, 2023.
- CMCC: ERA5 downscaling @2.2 km over Italy, <https://dds.cmcc.it/#/dataset/era5-downscaled-over-italy/hourly>, https://doi.org/https://doi.org/10.25424/cmcc/era5-2km_italy, accessed on 23rd February 2023, 2021.
- Copernicus: Copernicus Digital Elevation Model, <https://registry.opendata.aws/copernicus-dem>, accessed: 2nd February 2023, 2023.
- Csiszar, I.: *I*-Divergence Geometry of Probability Distributions and Minimization Problems, *The Annals of Probability*, 3, 146 – 158, <https://doi.org/10.1214/aop/1176996454>, 1975.
- Dhariwal, P. and Nichol, A. Q.: Diffusion Models Beat GANs on Image Synthesis, in: *Advances in Neural Information Processing Systems*, edited by Beygelzimer, A., Dauphin, Y., Liang, P., and Vaughan, J. W., <https://openreview.net/forum?id=AAWuCVzaVt>, 2021.
- Esser, P., Rombach, R., and Ommer, B.: Taming Transformers for High-Resolution Image Synthesis, in: *Proceedings of the IEEE/CVF Conference on Computer Vision and Pattern Recognition (CVPR)*, pp. 12 873–12 883, 2021.
- Falcon, W. and The PyTorch Lightning team: PyTorch Lightning, <https://doi.org/10.5281/zenodo.3828935>, 2019.
- Franch, G., Tomasi, E., and Cristoforetti, M.: DSIP-FBK/DiffScaler: LDM_res v1.0, <https://doi.org/10.5281/zenodo.13356322>, 2024.
- Giorgi, F., Jones, C., and Asrar, G. R.: Addressing climate information needs at the regional level: the Cordex framework, *World Meteorological Organization (WMO) Bulletin*, 58, 175, 2009.
- Goodfellow, I., Pouget-Abadie, J., Mirza, M., Xu, B., Warde-Farley, D., Ozair, S., Courville, A., and Bengio, Y.: Generative adversarial nets, *Advances in neural information processing systems*, 27, 2014.
- Goodfellow, I., Pouget-Abadie, J., Mirza, M., Xu, B., Warde-Farley, D., Ozair, S., Courville, A., and Bengio, Y.: Generative adversarial networks, *Commun. ACM*, 63, 139–144, <https://doi.org/10.1145/3422622>, 2020.

- Guibas, J., Mardani, M., Li, Z., Tao, A., Anandkumar, A., and Catanzaro, B.: Efficient Token Mixing for Transformers via Adaptive Fourier Neural Operators, in: International Conference on Learning Representations, <https://openreview.net/forum?id=EXHG-A3jIM>, 2022.
- Harris, L., McRae, A. T. T., Chantry, M., Dueben, P. D., and Palmer, T. N.: A Generative Deep Learning Approach to Stochastic Downscaling of Precipitation Forecasts, *Journal of Advances in Modeling Earth Systems*, 14, e2022MS003120, <https://doi.org/https://doi.org/10.1029/2022MS003120>, e2022MS003120 2022MS003120, 2022.
- Hersbach, H., Bell, B., Berrisford, P., Hirahara, S., Horányi, A., Muñoz-Sabater, J., Nicolas, J., Peubey, C., Radu, R., Schepers, D., Simmons, A., Soci, C., Abdalla, S., Abellan, X., Balsamo, G., Bechtold, P., Biavati, G., Bidlot, J., Bonavita, M., De Chiara, G., Dahlgren, P., Dee, D., Diamantakis, M., Dragani, R., Flemming, J., Forbes, R., Fuentes, M., Geer, A., Haimberger, L., Healy, S., Hogan, R. J., Hólm, E., Janisková, M., Keeley, S., Laloyaux, P., Lopez, P., Lupu, C., Radnoti, G., de Rosnay, P., Rozum, I., Vamborg, F., Villaume, S., and Thépaut, J.-N.: The ERA5 global reanalysis, *Quarterly Journal of the Royal Meteorological Society*, 146, 1999–2049, <https://doi.org/https://doi.org/10.1002/qj.3803>, 2020.
- Hersbach, H., Bell, B., Berrisford, P., Biavati, G., Horányi, A., Muñoz Sabater, J., Nicolas, J., Peubey, C., Radu, R., Rozum, I., Schepers, D., Simmons, A., Soci, C., Dee, D., and Thépaut, J.-N.: ERA5 hourly data on pressure levels from 1940 to present, <https://doi.org/10.24381/cds.bd0915c6>, accessed on 23rd February 2023, 2023a.
- Hersbach, H., Bell, B., Berrisford, P., Biavati, G., Horányi, A., Muñoz Sabater, J., Nicolas, J., Peubey, C., Radu, R., Rozum, I., Schepers, D., Simmons, A., Soci, C., Dee, D., and Thépaut, J.-N.: ERA5 hourly data on single levels from 1940 to present, <https://doi.org/10.24381/cds.adbb2d47>, accessed on 23rd February 2023, 2023b.
- Hewitson, B. and Crane, R.: Climate downscaling: techniques and application, *Climate Research*, 07, 85–95, <https://doi.org/10.3354/cr007085>, 1996.
- Höhlein, K., Kern, M., Hewson, T., and Westermann, R.: A comparative study of convolutional neural network models for wind field downscaling, *Meteorological Applications*, 27, e1961, <https://doi.org/https://doi.org/10.1002/met.1961>, 2020.
- Ioffe, S. and Szegedy, C.: Batch normalization: accelerating deep network training by reducing internal covariate shift, in: Proceedings of the 32nd International Conference on International Conference on Machine Learning - Volume 37, ICML'15, p. 448–456, JMLR.org, 2015.
- Isola, P., Zhu, J.-Y., Zhou, T., and Efros, A. A.: Image-To-Image Translation With Conditional Adversarial Networks, in: Proceedings of the IEEE Conference on Computer Vision and Pattern Recognition (CVPR), 2017.
- Jacob, D., Petersen, J., Eggert, B., Alias, A., Christensen, O. B., Bouwer, L. M., Braun, A., Colette, A., Déqué, M., Georgievski, G., et al.: EURO-CORDEX: new high-resolution climate change projections for European impact research, *Regional environmental change*, 14, 563–578, 2014.
- Kullback, S. and Leibler, R. A.: On Information and Sufficiency, *The Annals of Mathematical Statistics*, 22, 79 – 86, <https://doi.org/10.1214/aoms/1177729694>, 1951.
- Leinonen, J., Nerini, D., and Berne, A.: Stochastic Super-Resolution for Downscaling Time-Evolving Atmospheric Fields With a Generative Adversarial Network, *IEEE Transactions on Geoscience and Remote Sensing*, 59, 7211–7223, <https://doi.org/10.1109/TGRS.2020.3032790>, 2021.
- Leinonen, J., Hamann, U., Nerini, D., Germann, U., and Franch, G.: Latent diffusion models for generative precipitation nowcasting with accurate uncertainty quantification, 2023.
- Li, L., Carver, R., Lopez-Gomez, I., Sha, F., and Anderson, J.: Generative emulation of weather forecast ensembles with diffusion models, *Science Advances*, 10, eadk4489, <https://doi.org/10.1126/sciadv.adk4489>, 2024.

- Loshchilov, I. and Hutter, F.: Decoupled Weight Decay Regularization, in: International Conference on Learning Representations, <https://openreview.net/forum?id=Bkg6RiCqY7>, 2019.
- Maraun, D. and Widmann, M.: Statistical Downscaling and Bias Correction for Climate Research, Cambridge University Press, 2018.
- Mardani, M., Brenowitz, N., Cohen, Y., Pathak, J., Chen, C.-Y., Liu, C.-C., Vahdat, A., Kashinath, K., Kautz, J., and Pritchard, M.: Residual Diffusion Modeling for Km-scale Atmospheric Downscaling, 2023.
- Mescheder, L., Geiger, A., and Nowozin, S.: Which Training Methods for GANs do actually Converge?, 2018.
- Panofsky, H. and Brier, G.: Some Applications of Statistics to Meteorology, Earth and Mineral Sciences Continuing Education, College of Earth and Mineral Sciences, <https://books.google.it/books?id=1WARAQAAIAAJ>, 1968.
- Pathak, J., Subramanian, S., Harrington, P., Raja, S., Chattopadhyay, A., Mardani, M., Kurth, T., Hall, D., Li, Z., Aizzadenesheli, K., Hassanzadeh, P., Kashinath, K., and Anandkumar, A.: FourCastNet: A Global Data-driven High-resolution Weather Model using Adaptive Fourier Neural Operators, 2022.
- Peifer, H.: European Environmental Agency Reference Grid, <https://www.eea.europa.eu/data-and-maps/data/eea-reference-grids-2>, 2018.
- Price, I. and Rasp, S.: Increasing the accuracy and resolution of precipitation forecasts using deep generative models, <https://arxiv.org/abs/2203.12297>, 2022.
- Pulkkinen, S., Nerini, D., Pérez Hortal, A. A., Velasco-Forero, C., Seed, A., Germann, U., and Foresti, L.: Pysteps: an open-source Python library for probabilistic precipitation nowcasting (v1.0), Geoscientific Model Development, 12, 4185–4219, <https://doi.org/10.5194/gmd-12-4185-2019>, 2019.
- Raffa, M., Reder, A., Marras, G. F., Mancini, M., Scipione, G., Santini, M., and Mercogliano, P.: VHR-REA_IT Dataset: Very High Resolution Dynamical Downscaling of ERA5 Reanalysis over Italy by COSMO-CLM, Data, 6, <https://doi.org/10.3390/data6080088>, 2021.
- Rampal, N., Gibson, P. B., Sood, A., Stuart, S., Fauchereau, N. C., Brandolino, C., Noll, B., and Meyers, T.: High-resolution downscaling with interpretable deep learning: Rainfall extremes over New Zealand, Weather and Climate Extremes, 38, 100525, <https://doi.org/https://doi.org/10.1016/j.wace.2022.100525>, 2022.
- Rombach, R., Blattmann, A., Lorenz, D., Esser, P., and Ommer, B.: High-Resolution Image Synthesis with Latent Diffusion Models, CoRR, abs/2112.10752, <https://arxiv.org/abs/2112.10752>, 2021.
- Ronneberger, O., Fischer, P., and Brox, T.: U-Net: Convolutional Networks for Biomedical Image Segmentation, in: Medical Image Computing and Computer-Assisted Intervention – MICCAI 2015, edited by Navab, N., Hornegger, J., Wells, W. M., and Frangi, A. F., pp. 234–241, Springer International Publishing, Cham, ISBN 978-3-319-24574-4, 2015.
- Saharia, C., Ho, J., Chan, W., Salimans, T., Fleet, D. J., and Norouzi, M.: Image Super-Resolution via Iterative Refinement, IEEE Transactions on Pattern Analysis and Machine Intelligence, 45, 4713–4726, <https://doi.org/10.1109/TPAMI.2022.3204461>, epub 2023 Mar 7, 2023.
- Salimans, T. and Ho, J.: Progressive Distillation for Fast Sampling of Diffusion Models, CoRR, abs/2202.00512, <https://arxiv.org/abs/2202.00512>, 2022.
- Seity, Y., Brousseau, P., Malardel, S., Hello, G., Bénard, P., Bouttier, F., Lac, C., and Masson, V.: The AROME-France Convective-Scale Operational Model, Monthly Weather Review, 139, 976 – 991, <https://doi.org/10.1175/2010MWR3425.1>, 2011.
- Sharifi, E., Saghafian, B., and Steinacker, R.: Downscaling Satellite Precipitation Estimates With Multiple Linear Regression, Artificial Neural Networks, and Spline Interpolation Techniques, Journal of Geophysical Research: Atmospheres, 124, 789–805, <https://doi.org/https://doi.org/10.1029/2018JD028795>, 2019.
- Sohl-Dickstein, J., Weiss, E. A., Maheswaranathan, N., and Ganguli, S.: Deep Unsupervised Learning using Nonequilibrium Thermodynamics, 2015.

- Sperati, S., Alessandrini, S., D'Amico, F., Cheng, W., Rozoff, C. M., Bonanno, R., Lacavalla, M., Aiello, M., Airoidi, D., Amaranto, A., Decimi, G., and Vergata, M. A.: A new Wind Atlas to support the expansion of the Italian wind power fleet, *Wind Energy*, 27, 298–316, <https://doi.org/https://doi.org/10.1002/we.2890>, 2024.
- Stengel, K., Glaws, A., Hettlinger, D., and King, R. N.: Adversarial Super-resolution of Climatological Wind and Solar Data, *Proceedings of the National Academy of Sciences*, 117, 16 805–16 815, <https://doi.org/https://doi.org/10.1073/pnas.1918964117>, 2020.
- Stephan, K., Klink, S., and Schraff, C.: Assimilation of radar-derived rain rates into the convective-scale model COSMO-DE at DWD, *Quarterly Journal of the Royal Meteorological Society*, 134, 1315–1326, <https://doi.org/https://doi.org/10.1002/qj.269>, 2008.
- Tomasi, E., Franch, G., and Cristoforetti, M.: Sample dataset for the models trained and tested in the paper 'Can AI be enabled to dynamical downscaling? Training a Latent Diffusion Model to mimic km-scale COSMO-CLM downscaling of ERA5 over Italy', <https://doi.org/10.5281/zenodo.12934521>, 2024a.
- Tomasi, E., Franch, G., and Cristoforetti, M.: Pretrained models presented in the paper 'Can AI be enabled to dynamical downscaling? Training a Latent Diffusion Model to mimic km-scale COSMO-CLM downscaling of ERA5 over Italy', <https://doi.org/10.5281/zenodo.12941117>, 2024b.
- Tomasi, E., Franch, G., and Cristoforetti, M.: 2000-2002 Dataset [1/7] for the models trained and tested in the paper 'Can AI be enabled to dynamical downscaling? Training a Latent Diffusion Model to mimic km-scale COSMO-CLM downscaling of ERA5 over Italy', <https://doi.org/10.5281/zenodo.12944960>, 2024c.
- Tomasi, E., Franch, G., and Cristoforetti, M.: 2003-2005 Dataset [2/7] for the models trained and tested in the paper 'Can AI be enabled to dynamical downscaling? Training a Latent Diffusion Model to mimic km-scale COSMO-CLM downscaling of ERA5 over Italy', <https://doi.org/10.5281/zenodo.12945014>, 2024d.
- Tomasi, E., Franch, G., and Cristoforetti, M.: 2006-2008 Dataset [3/7] for the models trained and tested in the paper 'Can AI be enabled to dynamical downscaling? Training a Latent Diffusion Model to mimic km-scale COSMO-CLM downscaling of ERA5 over Italy', <https://doi.org/10.5281/zenodo.12945028>, 2024e.
- Tomasi, E., Franch, G., and Cristoforetti, M.: 2009-2011 Dataset [4/7] for the models trained and tested in the paper 'Can AI be enabled to dynamical downscaling? Training a Latent Diffusion Model to mimic km-scale COSMO-CLM downscaling of ERA5 over Italy', <https://doi.org/10.5281/zenodo.12945040>, 2024f.
- Tomasi, E., Franch, G., and Cristoforetti, M.: 2012-2014 Dataset [5/7] for the models trained and tested in the paper 'Can AI be enabled to dynamical downscaling? Training a Latent Diffusion Model to mimic km-scale COSMO-CLM downscaling of ERA5 over Italy', <https://doi.org/10.5281/zenodo.12945050>, 2024g.
- Tomasi, E., Franch, G., and Cristoforetti, M.: 2015-2017 Dataset [6/7] for the models trained and tested in the paper 'Can AI be enabled to dynamical downscaling? Training a Latent Diffusion Model to mimic km-scale COSMO-CLM downscaling of ERA5 over Italy', <https://doi.org/10.5281/zenodo.12945058>, 2024h.
- Tomasi, E., Franch, G., and Cristoforetti, M.: 2018-2020 Dataset [7/7] for the models trained and tested in the paper 'Can AI be enabled to dynamical downscaling? Training a Latent Diffusion Model to mimic km-scale COSMO-CLM downscaling of ERA5 over Italy', <https://doi.org/10.5281/zenodo.12945066>, 2024i.
- Vandal, T., Kodra, E., Ganguly, S., Michaelis, A., Nemani, R., and Ganguly, A. R.: DeepSD: Generating High Resolution Climate Change Projections through Single Image Super-Resolution, in: *Proceedings of the 23rd ACM SIGKDD International Conference on Knowledge Discovery and Data Mining, KDD '17*, p. 1663–1672, Association for Computing Machinery, New York, NY, USA, ISBN 9781450348874, <https://doi.org/10.1145/3097983.3098004>, 2017.

- von Storch, H., Zorita, E., and Cubasch, U.: Downscaling of Global Climate Change Estimates to Regional Scales: An Application to Iberian Rainfall in Wintertime, *Journal of Climate*, 6, 1161 – 1171, [https://doi.org/10.1175/1520-0442\(1993\)006<1161:DOGCCE>2.0.CO;2](https://doi.org/10.1175/1520-0442(1993)006<1161:DOGCCE>2.0.CO;2), 1993.
- Wang, J., Liu, Z., Foster, I., Chang, W., Kettimuthu, R., and Kotamarthi, V. R.: Fast and accurate learned multiresolution dynamical downscaling for precipitation, *Geoscientific Model Development*, 14, 6355–6372, <https://doi.org/10.5194/gmd-14-6355-2021>, 2021.
- Wilby, R. and Wigley, T.: Downscaling general circulation model output: a review of methods and limitations, *Progress in Physical Geography: Earth and Environment*, 21, 530–548, <https://doi.org/10.1177/030913339702100403>, 1997.
- Yadan, O.: Hydra - A framework for elegantly configuring complex applications, Github, <https://github.com/facebookresearch/hydra>, 2019.